Stable Surface-based Turbulent Layer during the Polar Winter at Dome C, Antarctica: Sodar and In Situ Observations

Igor Petenko[1,2] • Stefania Argentini[1] • Giampietro Casasanta[1] • Christophe Genthon[3] • Margarita Kallistratova[2]

Received: DD Month YEAR /Accepted: DD Month YEAR

Abstract An experiment to investigate atmospheric turbulence was performed at Concordia station (Dome C, Antarctica) during winter 2012, finding significant turbulence in a near-surface layer extending to heights of a few tens of metres, despite the strong stable stratification. The spatial and temporal behaviour of thermal turbulence was examined using a high-resolution sodar, starting from the lowest few metres with a vertical resolution better than 2 m. Sodar observations were complemented by in situ measurements using a weather station and radiometers near the surface, temperature and wind-speed sensors at six levels on a 45-m tower, and radiosondes. The depth of the surface-based turbulent layer (SBTL) at Dome C during the whole winter was directly measured experimentally for the first time, and had an average depth of ≈ 23 m, varying from a few to several tens of metres, while the inversion-layer depth was ≈ 380 m. Relationships between the depth of the SBTL and atmospheric parameters such as the temperature, wind speed, longwave radiation, Brunt–Väisälä frequency and Richardson number are shown. The SBTL under steady weather conditions is analyzed and classified into three prevailing types: 1) a very shallow layer with a depth < 15 m, 2) a shallow layer of depth 15–70 m with uniform internal structure, 3) a shallow layer of depth 20–70 m with waves. Wave activity in the SBTL was

✉ Igor Petenko
i.petenko@isac.cnr.it

[1] Institute of Atmospheric Sciences and Climate, CNR, Rome, Italy

[2] A.M. Obukhov Institute of Atmospheric Physics RAS, Moscow, Russia

[3] Laboratoire de Meteolorogie Dynamique, CNRS, Paris, France

observed during a significant portion of the time, with sometimes regular (with periodicity of 8–15 min) trains of Kelvin–Helmholtz billow-like waves occurring at periods of 20–60 s, and lasting several hours.

Keywords Dome C Antarctica • Internal gravity–shear waves • High-resolution sodar • Stable boundary layer • Surface-based turbulent layer

1 Introduction

We report and categorize the important features of small-scale turbulence and sub-mesoscale structures in the stably-stratified atmospheric boundary layer (SBL) under strong background stability caused by large temperature gradients at extremely low temperatures during the polar winter on the high Antarctic plateau. A common agreement on the necessity to improve the description of dynamic and turbulent processes in the SBL has been recently reached. Although the research of the SBL has been performed for several decades, a unified pattern or theory does not exist, and the characteristics and origin of turbulence within the SBL are not yet well clarified. The accurate determination of turbulent transfer in the lower atmosphere is important for the improved understanding of surface–atmosphere exchange processes, as well as for improving their representation in numerical-weather and air-quality-prediction models, especially in the polar regions. The knowledge of atmospheric turbulence properties is also important to quantify their influence on the distortion of astronomical images (Gur'yanov et al. 1992; Petenko et al. 2014) and the propagation of electromagnetic waves for telecommunication purposes (e.g. Tatarskii 1971).

Different classifications of stable-layer regimes have been suggested in the literature, beginning from the simplest two-regime classification to multi-regime ones of up to five regimes. Detailed reviews of studies of the SBL are found in Salmond and McKendry (2005), Banta (2008), Mahrt (2014), and Sun et al. (2015). Different variables have been suggested as a stability parameter to classify different types of SBL, including h/L (e.g. Nieuwstadt 1984; Holtslag and Nieuwstadt 1986) and z/L (e.g. Mahrt et al. 1998; Mahrt 1999), where z is the height above the surface, h is the height of the SBL, and L is the surface-layer Obukhov length. Grachev et al. (2005), who analyzed data obtained over the Arctic ice, showed that the SBL can be classified into four major regimes: the (i) surface-layer-scaling regime (weakly stable case), (ii) transition regime, (iii) turbulent Ekman layer, and (iv) intermittently-turbulent Ekman layer (supercritical stable regime). The use of a Richardson number (both gradient and bulk) for scaling has been discussed by Van de Wiel et al. (2002a), Klipp and Mahrt (2004), Grachev et al. (2005, 2013), Mahrt and Vickers (2006), Baas et al. (2006), Galperin et al. (2007), Sorbjan (2006, 2010), Mahrt et al. (2012), and Sorbjan and Grachev (2010), among others. As a less noisy estimate of the background stability, Kitaigorodskii and Joffre (1988) and Joffre et al. (2001) suggested using for the height h a length scale u_* / N, where u_* is the surface friction velocity, and N is the Brunt–Väisälä frequency above h. Mironov and Fedorovich (2010) examined different formulations of the SBL depth, and proposed generalized depth-scale formulations. Van de Wiel et al. (2002a, b; 2003) used the surface turbulent fluxes and the surface net radiation R_{net} to separate the SBL into three regimes: the continuous-turbulence regime for the weakest stability, the intermittent regime, and the radiation regime for the strongest stability. Banta et al. (2002) used the mean low-level-jet speed to identify categories of SBL turbulence structure, while Mahrt and Vickers (2006) found a similar relationship using the mean wind speed at 2 m. Banta (2008) noted that, for many purposes, it is desirable to characterize the SBL turbulence in terms of the largest-scale external variables possible. Sun et al. (2012) revealed three turbulence regimes depending on the wind speed. Van Hooijdonk et al. (2015) characterized the SBL regimes by a new non-dimensional parameter, the shear capacity, enabling the prediction of different flow regimes. Petenko et al. (2014) showed the dependence of the sodar-measured depth of the turbulent layer at Dome C, Antarctica during winter on the wind speed at 3 m, which consists of two linear regions with different slopes intersecting at 3–4 m s^{-1}. Vignon et al. (2017a) identified two regimes of the temperature-gradient dependence on the 10-m wind speed with a threshold of ≈ 6 m s^{-1}, and emphasized that SBL dynamics are primarily driven by the wind shear.

While linear theory predicts that small-scale fluctuations only exist when the Richardson number Ri < the critical value of the Richardson number Ri_{cr} = 0.25 (e.g. Miles 1961; Howard 1961), in many geophysical flows, turbulence exists for Ri > 0.25 (e.g. Schumann and Gerz 1995). Observations show that there is no clear critical Richardson number for decaying turbulent fluxes (e.g. Galperin et al. 2007; Grachev et al. 2013).

Zilitinkevich et al. (2007) showed that a second-order moment closure model can predict the persistence of turbulence beyond the critical Richardson number.

Stable stratification favours the occurrence of disturbances other than turbulence, which are associated with sub-mesoscale or mesoscale motions, such as propagating buoyancy waves (internal gravity waves), vorticity-generated waves (Kelvin–Helmholtz billows), and solitary waves (Sun et al. 2004, 2015; Mahrt and Vickers 2006). Of the ground-based remote-sensing techniques for studying sub-mesoscale motions in the atmosphere, including waves, sodar is the simplest among them, and is most suitable for investigation of the shallow SBL. Sodar measures the temperature structure parameter C_T^2 characterizing the intensity of temperature fluctuations not only at one fixed level but continuously over a height range up to several hundreds of metres. The parameter C_T^2 is a proportionality factor in the two-thirds law for the structure function D_T, which is valid within the inertial subrange of locally-isotropic turbulence (Obukhov 1949)

$$D_T(r) = \overline{\left[T'(\mathbf{r}_1) - T'(\mathbf{r}_2)\right]^2} = C_T^2 r^{2/3}, \tag{1}$$

where $T'(\mathbf{r})$ is the temperature fluctuation around its mean at the point $\mathbf{r}$, and $r = |\mathbf{r}_1 - \mathbf{r}_2|$ is the distance between points $\mathbf{r}_1$ and $\mathbf{r}_2$.

In acoustic remote sensing, the parameter C_T^2 is determined from measurements of the intensity of the backscattered acoustic signal (Tatarskii 1971),

$$C_T^2 = 0.25 \times 10^3 T^2 k^{-1/3} \sigma_{180}, \tag{2}$$

where σ_{180} is the effective backscattering cross-section at a 180° angle per unit of scattering volume per unit solid angle, T is the absolute temperature of the air, and k is the acoustic wavenumber. More information about acoustic remote sensing can be found in Brown and Hall (1978). Even if a sodar is not calibrated, the relative values of C_T^2 provide useful information on the spatial and temporal variability of the thermal turbulence intensity. In fact, thermal turbulence is a perfect indicator of any sub-mesoscale disturbances being generated by them, so a sodar is able to visualize their morphology and help to determine what kind of mentioned phenomena occurs. Based on our experience with sodar observations, we believe it is not correct to consider separately small-scale turbulence and sub-mesoscale motions, which originate from large-scale features of a flow and the external conditions, and generate in turn local small-scale turbulence whose spatial and temporal distribution is modulated by the larger-scale motions. Sun et al. (2004) analyzed the generation of turbulence by different atmospheric disturbances. The problem of the separation between the turbulence and non-turbulent motions (Mahrt 2010) demands a priori information on the specific variability of temporal scales related to processes occurring under stable stratification. Preliminary experimental data from ground-based remote-sensing measurements can help develop appropriate analysis procedures to separate the effect of purely turbulent processes from larger-scale motions. Sodars (as well as radars and lidars) often show clear traces of wavelike structures appearing as undulating layers of enhanced thermal turbulence oscillating vertically (e.g. Gossard et al. 1970, 1985; Emmanuel et al. 1972; Hooke et al. 1973; Kallistratova and Petenko 1993; Petenko et al. 2012), which are very likely due to different kinds of atmospheric waves generated by various mechanisms, with the duration of wave motions varying from a few minutes to several hours. Waves generated by shear-flow instability are common in the SBL (Bretherton 1969; Sun et al. 2015; Lyulyukin et al. 2015). For example, in Antarctica, wavelike structures have been observed in several studies (King et al. 1987; Kouznetsov 2009; Neff et al. 2008; Petenko et al. 2013, 2015; Argentini et al. 2014b), and Petenko et al. (2016) reported wavelike braid (or herringbone) patterns in the turbulent layer occurring regularly during morning convection development at Dome C, Antarctica.

Adequate understanding of the turbulence in the SBL demands measurements of high vertical resolution, since turbulence can be confined in layers, sometimes only a few metres deep (Gossard et al. 1970, 1985; Kallistratova and Petenko 1993). Here, we present a qualitative description of the turbulence structure in the SBL under strong background stability, as observed during the polar winter at Dome C on the Antarctic plateau. The description of the experimental set-up and meteorological conditions is given in Sect. 2, and different patterns of the spatial and temporal distribution of turbulence observed by a high-resolution sodar are described in Sect. 3. The spatial and temporal characteristics of the turbulence structure in the lowermost (< 100 m) atmospheric layer are considered under different meteorological and stability conditions, focusing on the presence of wave activity. The summary is presented in Sect. 4.

2 Experimental Set-up and Meteorological Conditions

The experiment was carried out during the austral winter of 2012 at the French–Italian station of Concordia Dome C (75°06’’S, 123°21’’E), Antarctic plateau, East Antarctica (Fig. 1). The station elevation is 3233 m above sea level at a distance of 900 km inland from the nearest coast, with a surface slope at this site ≈ 0.1%. The sun culminates at 38° on 21 December, and is permanently below the horizon from 6 May to 12 August.

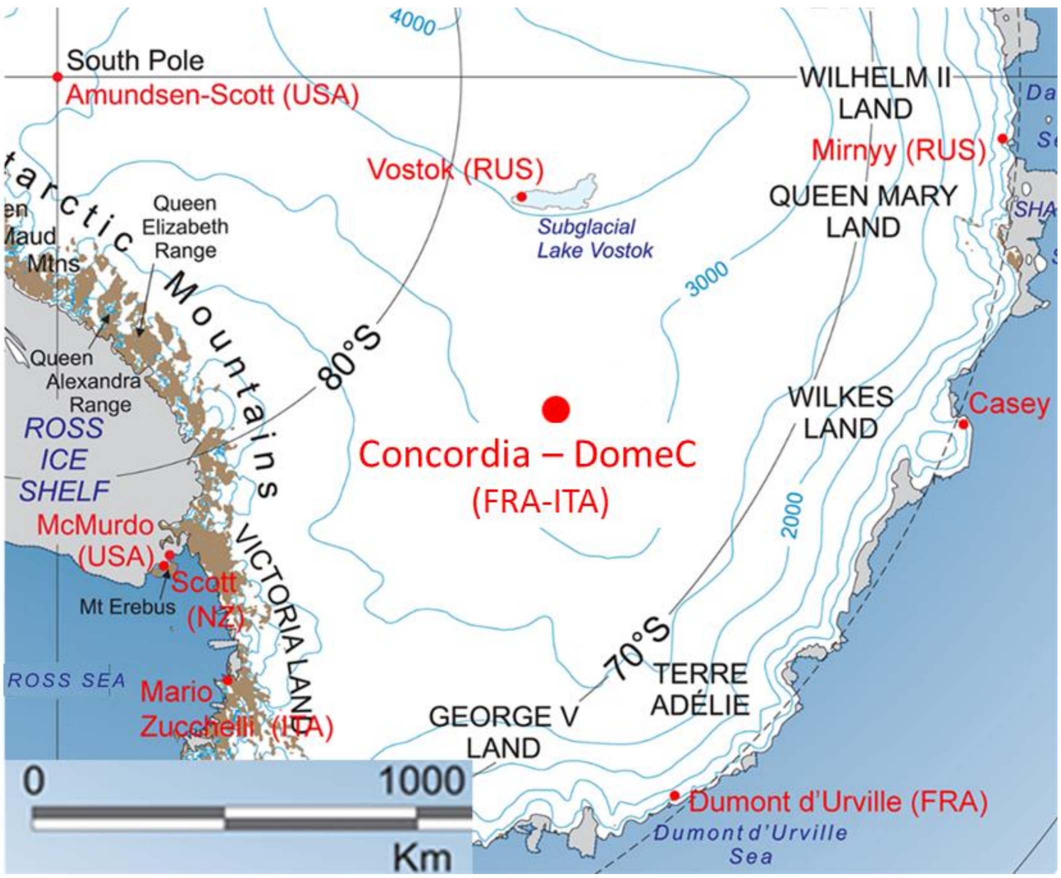

Fig. 1 Geographical map of East Antarctica, with the position of Dome C (red dot)

2.1 Instrumentation

2.1.1 Sodar System

An advanced version of a high-resolution sodar (Argentini et al. 2012) developed by the Institute of Atmospheric Sciences and Climate of the National Research Council of Italy (ISAC-CNR) was used for turbulence observations in the height range of 2–200 m. The four vertically-pointed sodar antennae (three transmitting and one receiving) were installed 400 m south-west of the main buildings of Concordia station (Fig. 2) to minimize the influence of the station considering that the prevailing atmospheric flow is from the south-south-west sector. The duration of the acoustic pulse emitted every 2 s is 10 ms, with a corresponding vertical extent of the scattering volume of 1.7 m. Instantaneous values of the echo intensity with a vertical step of < 1 m were recorded. Details on the processing techniques may be found in Argentini et al. (2012, 2014b). A noise-subtraction procedure was developed and applied to the echo-signal intensity profiles (Petenko et al. 2014) to increase the data quality. While measurements were performed during the entire winter period, as the sodar was used for several scientific tasks, the high-resolution measurements were only available during the second part of every month from April to September 2012, and continuously over 24 h for a total of ≈ 2500 h covering more than 80 days.

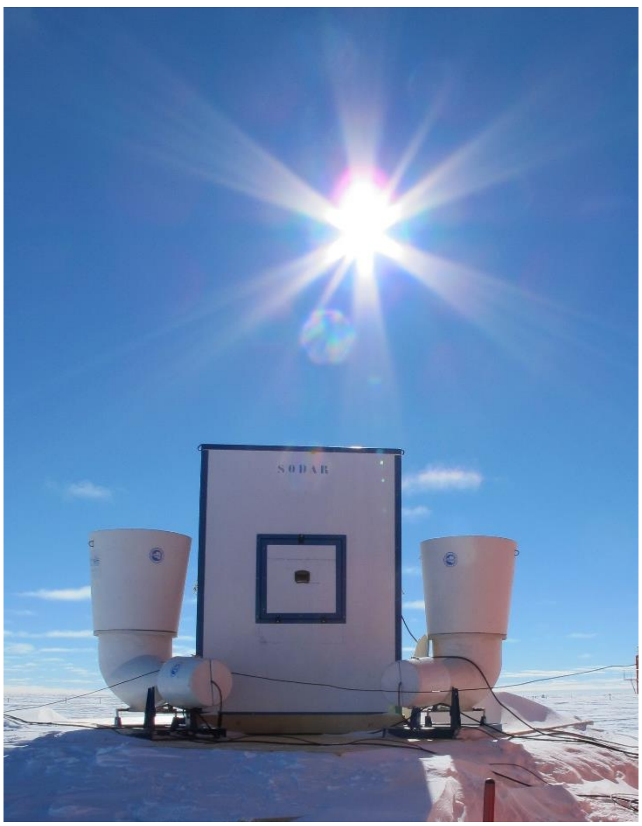

Fig. 2 Sodar antennae

2.1.2 Other Measurements

Measurements of air temperature, humidity, wind speed and direction were provided by an automatic weather station Milos 520 (Vaisala) with an acquisition rate of 1 min at heights of 1.4 and 3.6 m above the surface for the temperature and wind speed, respectively. A mast equipped with a net radiometer CNR1 (Kipp & Zonen) and an ultrasonic anemometer–thermometer USA-1 (Metek) at a height of 3.5 m was installed about 15 m from the sodar antennae. The value of the downwards longwave radiative flux > 75 W m^{-2} was used as an objective criterion for the presence of clouds or mist. Unfortunately, sonic measurements under low temperatures and weak turbulence had several technical limitations: (i) as the normal functionality of ultrasonic sensors is limited to temperatures > −40°C, a heating system is used to allow a functionality up to −50°C; however, this heating may disturb and increase the background turbulence, especially influencing temperature fluctuations and the heat flux. (ii) Another problem is caused by internal electronic noise, which is different for the wind speed and temperature channels, influencing mainly the temperature measurements. For this reason, in many cases, even if the momentum-flux (or friction velocity) measurements are reliable, the heat-flux measurements failed, making accurate determination of the Obukhov length L impossible under these circumstances.

Radiosoundings were performed every day at 1930 local standard time (LST = UTC + 8) with a radiosonde RS92-GSL (Vaisala) (temperature, humidity and wind-speed measurements). In addition, temperature and wind-speed profiles from a 45-m tower located at a distance of approximately 1 km were available (see Genthon et al. 2013 and Vignon et al. 2017a for a description of the tower equipment), yielding measurements at heights of about 3, 10, 17, 25, 32 and 41 m. To quantify the stability, we take the bulk Richardson number Ri_{B} as a stability parameter, and follow Mahrt and Vickers (2006) by computing the bulk Richardson number Ri_{B} between the levels z_1 and z_2 as

$$Ri_{\mathrm{B}} = \frac{g}{\theta_0}\frac{[\theta(z_2)-\theta(z_1)](z_2-z_1)}{[V(z_2)-V(z_1)]^2} , \tag{3}$$

where g is the acceleration due to gravity, z is the height above the surface, V is the wind speed, θ is the potential temperature in K calculated as $\theta(z) = T\,[1000/p(z)]^{0.286}$, where T is the absolute temperature in K, p is the air pressure in hPa, and θ_0 is the average value of θ between two levels.

The Brunt–Väisälä frequency is determined from

$$N^2 = \frac{g}{\theta_0}\frac{[\theta(z_2)-\theta(z_1)]}{(z_2 - z_1)}, \tag{4}$$

with the period corresponding to the Brunt–Väisälä frequency termed the “buoyancy period”, and calculated as $T_b = 2\pi\, N^{-1}$.

The snow-surface temperature T_s is retrieved from the radiometer data as in Vignon et al. (2017b) by

$$T_s = \left(\frac{LW\uparrow + (\varepsilon - 1)LW\downarrow}{\varepsilon\sigma}\right)^{1/4}, \tag{5}$$

where σ is the Stefan–Boltzmann constant, ε is the snow emissivity of 0.99 (Brun et al. 2011), and $LW\uparrow$ and $LW\downarrow$ are the upwards and downwards longwave radiative fluxes, respectively.

2.1.3 Characteristics of Meteorological Conditions

The histogram of temperature and the wind rose are shown in Fig. 3a and b, and are in reasonable agreement with the results of previous measurements (e.g. Genthon et al. 2013; Pietroni et al. 2012, 2014; Argentini et al. 2014a). The temperatures varied between −80 and −30°C, and the lowest temperatures (< −70°C) generally occurred under clear-sky conditions. The local climate is characterized by strong temperature inversions, whose strength, estimated as the difference between temperatures at the top of the inversion and near the surface, reaches 35°C. A histogram of inversion strength is shown in Fig. 3c, indicating negative skewness of the distribution and an average strength ≈ 23°C. The flow regime at ≈ 3 m is characterized mainly by low (< 4 m s^{-1}) and moderate (4–6 m s^{-1}) wind speeds. Low and moderate katabatic flows are from the south-south-west sector under cold, calm and fair weather conditions. Low wind speeds, which occurred 40% of the time, normally did not produce significant turbulence, while moderate wind speeds, which occurred 50% of the time, favoured enhanced turbulence in the lowest 10–50-m layer.

During winter, remarkable synoptic variations accompanied with cloudiness occurred due to intrusions of warm and moist air masses from the coastal zones, causing the asymmetry of the distributions of temperature and the inversion strength (Fig. 3a and b). These episodic (every 8–12 days) weather events are characterized by higher wind speeds (up to 12 m s^{-1}), significantly higher temperatures (up to −40°C), a decrease in the inversion strength, and strong cloudiness (e.g. Argentini et al. 2001; Genthon et al. 2013). Intense turbulence in the lowest 100-m layer and elevated turbulent layers at heights of several hundred metres were observed during transition periods.

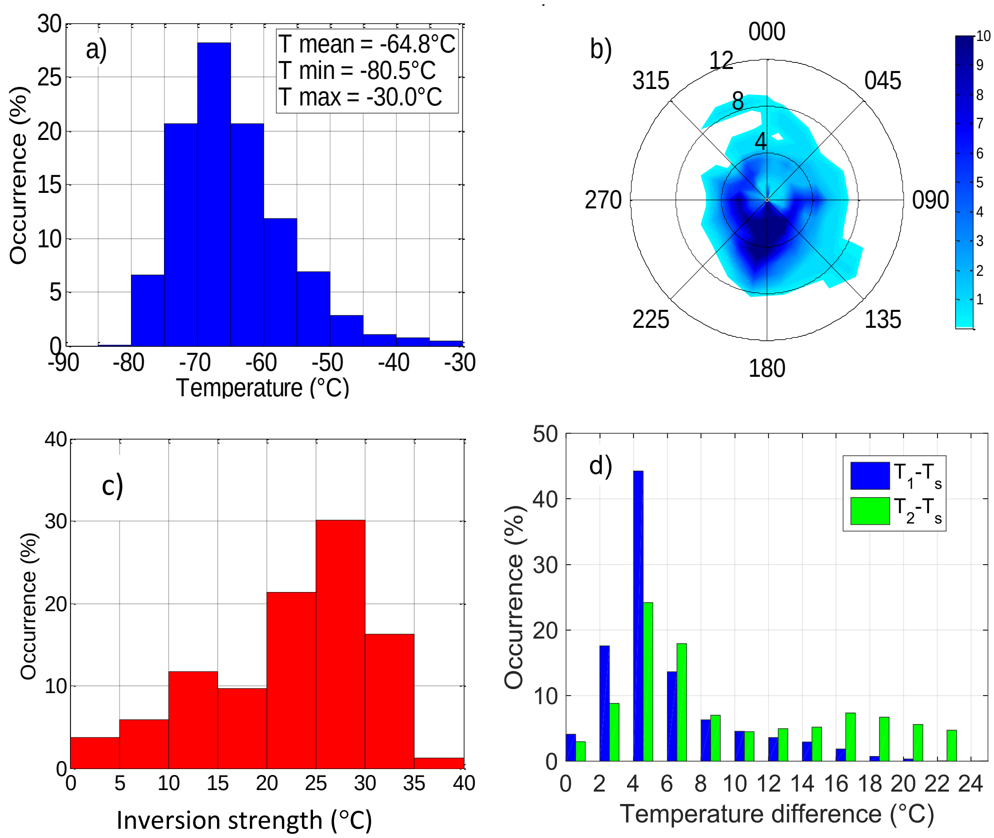

Fig. 3 Statistics of meteorological variables for the period April–September 2012. Histograms of **a** temperature at 1.4 m, **c** inversion strength from radiosonde ascents, and **d** differences between the temperature T_1 at 3 m and the snow-surface temperature T_s (blue), and between the temperature T_2 at 10 m and T_s (green). **b** Wind rose showing the joint probability of wind speed and direction at 3.6 m (the colour intensity is proportional to the value of the joint probability density function)

3 Results and Discussion

The results reported herein are minimally influenced by orography and other external factors, with the flat surface of slope of < 0.1% providing true horizontal homogeneity.

Due to the near absence of the sun during the considered period, diurnal variations are almost negligible. Periods of steady fair weather had a rather long duration of 5–10 days, being interrupted only by shorter episodic intrusions of warm air and cloudiness from coastal zones.

3.1 Surface-based Turbulent Layer

Based on visual inspection of sodar echograms and on the analysis of vertical profiles of the return-signal intensity for several months, we conclude that the altitude where turbulence occurs is not equivalent to the whole SBL, which sometimes is associated with a temperature inversion layer (Yamada 1976) or with a layer below the low-level-jet maximum (Melgarejo and Deardorff 1974). It has been shown theoretically by Garratt and Brost (1981), and experimentally by André and Mahrt (1982), that the depth of the turbulent layer can be less than the inversion-layer depth. Figure 4 shows an example of a sodar echogram and profiles of air temperature and wind speed measured on the 45-m tower and by a radiosonde on 27 August 2012, illustrating a time–height section of the logarithm of the structure parameter C_T^2 in arbitrary units. Turbulence occurs only in the lowest part (< 40–60 m in this case) of the temperature inversion layer. Although $Ri_\mathrm{B} > 0.25$ at the heights between 20 and 60 m (Fig. 4h), thermal turbulence is significant in this region. In the upper part (> 60 m) with high Ri_B values, no turbulence is detected.

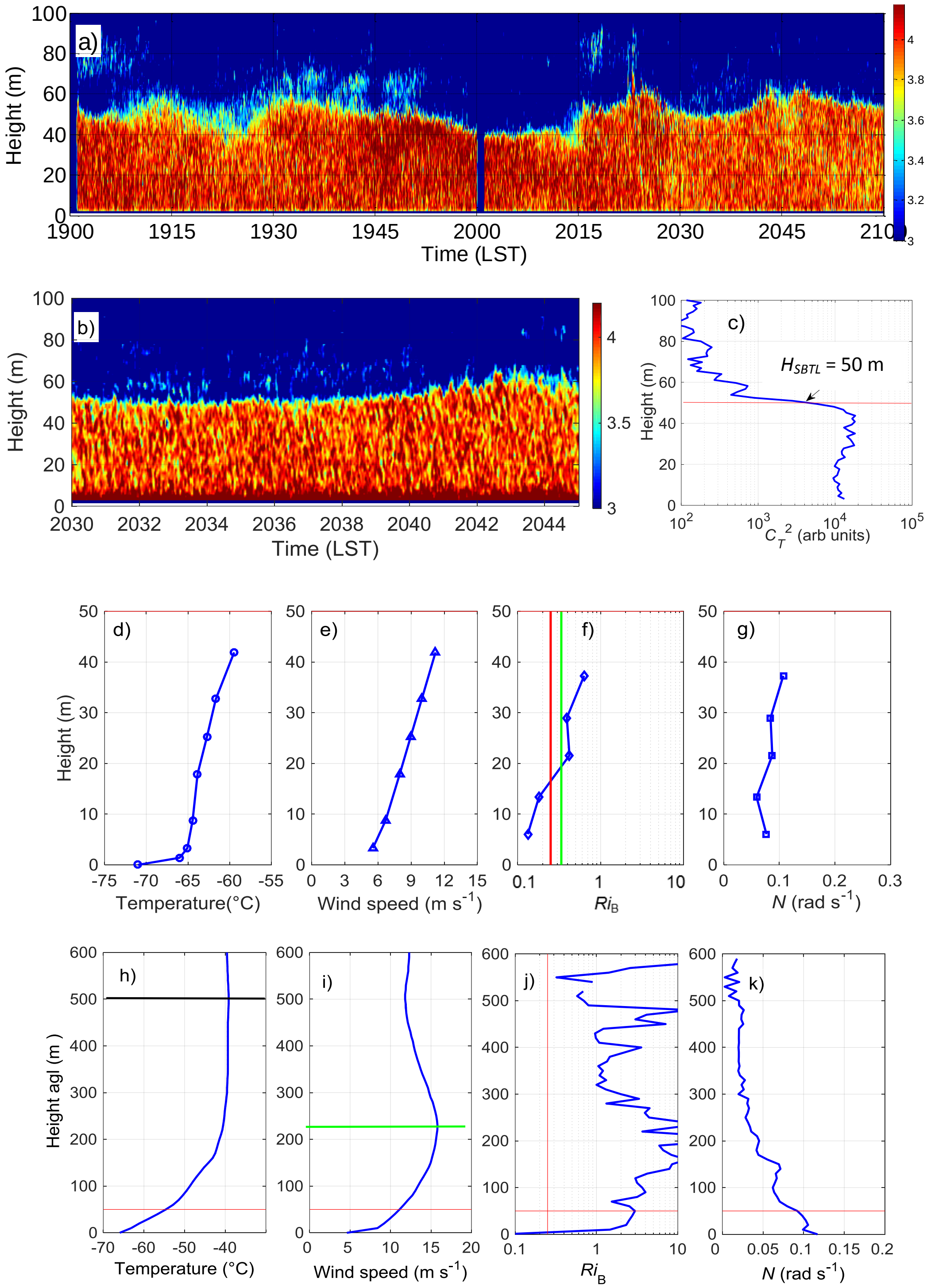

Fig. 4 Sodar echogram and profiles of meteorological parameters recorded on 27 August 2012, 1900–2100 LST. **a** Example of the SBTL shown by a sodar echogram; the colourbar shows the logarithm of the structure parameter C_T^2 (arbitrary units). **b** Detailed view of the echogram for the same day (2030–2045 LST). **c**

Vertical profiles of the parameter C_T^2 in arbitrary units (2030–2045 LST), **d** temperature, **e** wind speed, **f** Richardson number, and **g** Brunt–Väisälä frequency measured on the tower on 27 August 2014, 1900–2100 LST. Vertical profiles of **h** temperature, **i** wind speed, **j** Richardson number, and **k** Brunt–Väisälä frequency measured by a radiosonde on 27 August 2014, 1930 LST. The solid horizontal red lines in **c**–**k** indicate the average position of the top of the turbulent layer located at ≈ 50 m. The thick solid horizontal black line in **h** indicates the position of the top of the temperature inversion layer located at ≈ 500 m. The red vertical line in Fig. 4e shows Ri_B = 0.25. The green vertical line in **f** shows the bulk Richardson number Ri_B calculated between z_1= 3 m and z_2 = 41 m. The solid horizontal green line in **i** indicates the height of the wind-speed maximum at ≈ 230 m

Note that the largest gradients of temperature and wind speed occur within the turbulent layer; above the turbulent layer, the gradients decrease. The maximum temperature is reached at ≈ 500 m, and the wind speed increases from 6 m s^{-1} at 3.5 m to 16 m s^{-1} at 230 m. The sodar turbulence observations and temperature vertical profiles from tower and radiosonde measurements indicate a separate sub-layer within the entire SBL containing enhanced turbulence associated with a layer of temperature inversion. We focus on this atmospheric region, calling it a *surface-based turbulent layer* (hereafter, SBTL) to indicate a turbulent part of the SBL at the surface, which is a term first suggested in Seaman et al. (2002). Note, we use it only for stable stratification, and not for the convective boundary layer. The SBTL is clearly detected from sodar observations, and its top is easily determined due to the sharp cessation of thermal turbulence, where the value of C_T^2 decreases by one to two order of magnitudes over a few metres, as shown by Petenko et al. (2014). Due to a sharp decrease of C_T^2 values above the SBTL (Fig. 4c), the position of its upper boundary in sodar echograms is insensitive to the choice of colour scales. From the sodar records (Fig. 4a), it is possible to estimate the SBTL depth (H_{SBTL}) visually as a height of the boundary of the coloured (or black) band in echograms. Moreover, other methods for determining the mixing height in the atmospheric boundary layer (ABL) from sodar C_T^2 (or, reflectivity) profiles (e.g. Beyrich 1997; Casasanta et al. 2014) also give unambiguous values of H_{SBTL}. We believe that the depth of the SBTL, being determined directly experimentally, plays a key role in the parametrization of the SBL, as well as in the verification of modelling results.

Variations of depth H_{SBTL} during the observational period are shown in Fig. 5 together with the temperature inversion height (H_{INV}) and the height of the wind-speed maximum (H_{Vmax}) determined from radiosonde measurements. Usually, the height of the temperature inversion layer is defined as the position of the maximum value in the temperature profile. However, often in practice, as an estimate of the temperature inversion height, one takes a height where the temperature gradient passes a certain threshold, making the estimate of the inversion height H_{INV} dependent on the criteria used. Shown in Fig. 5 are time variations of H_{INV} values estimated from the temperature maximum and from the temperature-gradient threshold based on the value of the temperature gradient equal to 0.005 K m^{-1} as in Drue and Heinemann (2007). Large differences between the H_{INV} and H_{SBTL} values are evident, which is consistent with that reported previously (Garratt and Brost 1981; André and Mahrt 1982; Drue and Heinemann 2007). While Drue and Heinemann (2007) determined the height of the turbulent SBL as a height of the maximum wind speed H_{Vmax}, in our measurements, the H_{SBTL} values at Dome C are much less than the height of the wind-speed maximum. No correlation between either the depths H_{SBTL} and H_{INV} or the depths H_{SBTL} and H_{Vmax} was found (not shown).

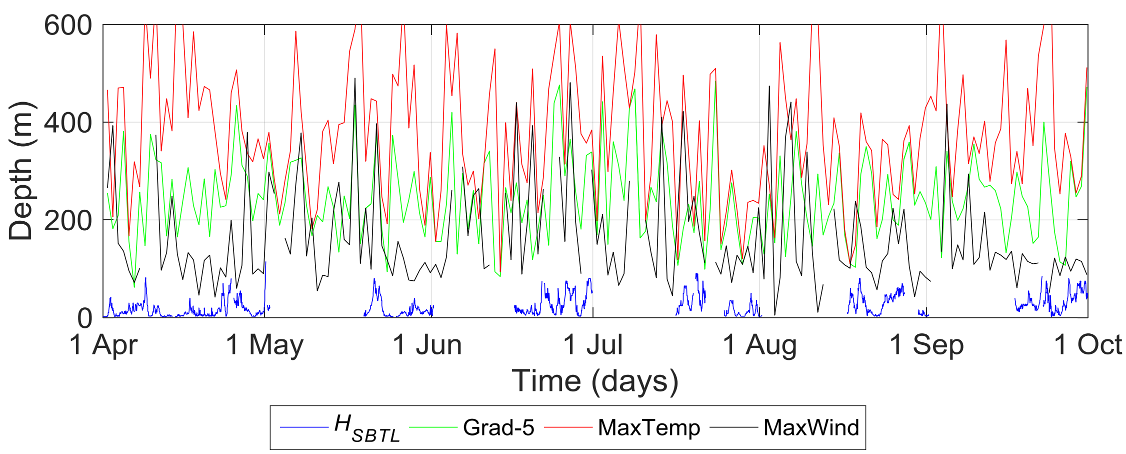

Fig. 5 Time series of (i) 1-h-averaged depth H_{SBTL} as estimated from sodar echograms (blue), and (ii) inversion heights H_{INV} determined from the position of the temperature maximum (red) and from the height where the temperature gradient reaches the threshold equal to 0.005 K m^{-1} (green), and the height of the low-level wind-speed maximum H_{Vmax} (black) from 1 April to 30 September 2012

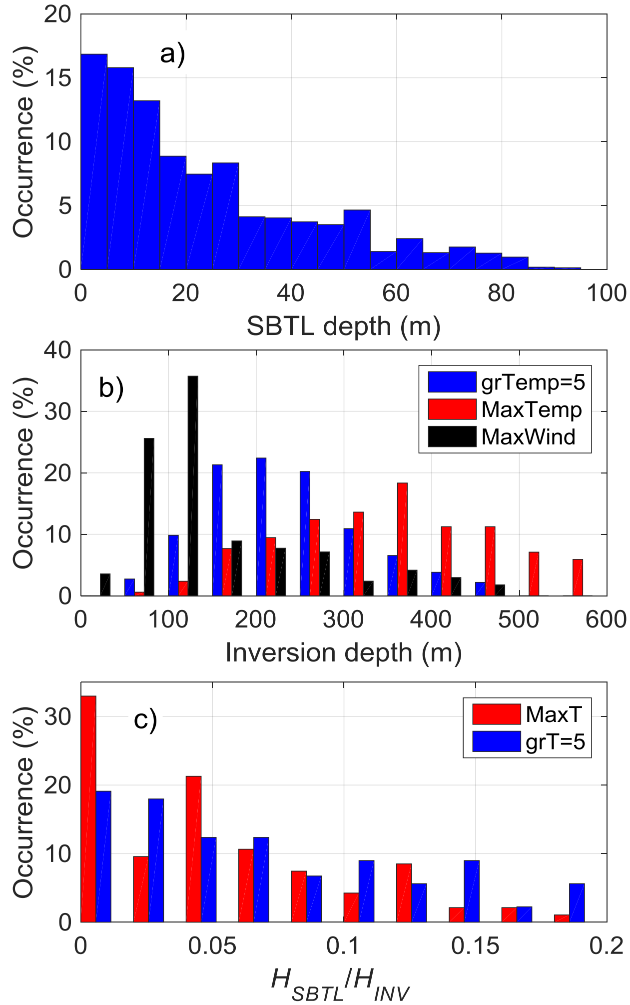

Fig. 6 Histograms of the depths **a** H_{SBTL} (from sodar), **b** H_{INV} and H_{Vmax} (from radiosonde), **c** and the ratio H_{SBTL} / H_{INV} (*red* – H_{INV} from the height of the temperature maximum, *blue* – H_{INV} from the height where the temperature gradient is equal to 0.005 K m^{-1}) for April–September 2012

The histogram of depths H_{SBTL} shown in Fig. 6a indicates that values H_{SBTL} > 20 m (< 20 m) are observed for 45% (55%) of the total observational period, while values H_{SBTL} < 5 m for 17% of the period. Particularly deep layers where H_{SBTL} > 70 m are observed 5% of the time, and these are mainly associated with weather changes. Figure 6b shows the histogram of (i) the depth H_{INV} estimated by the maximum temperature (red) and from the gradient equal to 0.005°C m^{-1} (blue), and (ii) the depth H_{Vmax} (black). The statistics of the depth H_{SBTL}, the values of H_{INV} estimated with different criteria, and the depth H_{Vmax} are given in Table 1.

Table 1. The depth of the SBTL, and the heights of the temperature inversion layer and wind-speed maximum averaged over the period April–September 2012.

Depth (m)	Mean (m)	Median (m)	Standard deviation (m)
Turbulence layer	23	16	20
Inversion layer (Temperature maximum)	380	367	140
Inversion layer (Temperature gradient = 0.005 K m^{-1})	244	235	88
Height of the wind-speed maximum	162	123	104

The mean SBTL depth is 23 m, while the inversion-layer depth (the height of the temperature maximum) is 380 m. The wind-speed maximum occurs on average at a height of ≈ 160 m, which is considerably lower than the depth H_{INV}. The probability distribution of the ratio H_{SBTL} / H_{INV} shown in Fig. 6c has a wide range of variability. In half of the cases, the SBTL occupies less than 5% of the inversion layer. Stable boundary layers less than a few tens of metres deep have been found during very stable conditions with weak wind speeds and classified as shallow layers (e.g. Smedman 1988; Mahrt and Vickers 2006; Grachev et al. 2013). The SBTL observed in our experiment may also generally be considered as shallow.

Figure 7 shows the relationship between the depth H_{SBTL} and different meteorological and turbulent parameters for the period April–September 2012. In Fig. 7a, H_{SBTL} values are plotted versus temperature, with the colours of circles representing the wind speed. The smaller values of H_{SBTL} < 10 m are observed mainly at temperatures < −60°C, when wind speeds are < 4 m s^{-1}; layers deeper than 50 m, in practice, are not observed at temperatures

< −70°C. However, a clear correlation between the depth H_{SBTL} and temperature is absent. Figure 7b shows the depth H_{SBTL} versus the 3.6-m wind speed with colours representing the temperature, importantly illustrating that the value of H_{SBTL} increases with the wind speed, which may be approximated by lines of different slopes intersecting at 3–4 m s^{-1}. A similar feature was found by Vignon et al. (2017a) for the relationship between the friction velocity u_* and the 10-m wind speed with the intersection point around 6 m s^{-1}. In our case, when the 3-m wind speed > 4 m s^{-1}, then usually the value of H_{SBTL} > 20 m for a wide range of temperatures. The relationship between the depth H_{SBTL} (in m) and wind speed V (in m s^{-1}) can be roughly estimated as $H_{SBTL} \approx 12V - 10$ for $V > 3$ m s^{-1}.

The depth H_{SBTL} versus the longwave downwards radiation and the difference between the longwave upwards and downwards radiation are plotted in Fig. 7c and d, respectively, with the colour scale representing the wind speed, illustrating no simple dependence between the depth H_{SBTL} and radiation characteristics. From Fig. 7c, we conclude that the value of H_{SBTL} does not depend on the downwards longwave radiation $LW\downarrow$, but is influenced mainly by the wind speed. From Fig. 7d, it is seen that the lowest depths H_{SBTL} < 20 m occur mainly for low wind speeds < 3 m s^{-1}, with the difference $LW\uparrow - LW\downarrow$ lying between 15 and 20 W m^{-2}; values of H_{SBTL} > 20 m occur for the differences $LW\uparrow - LW\downarrow$ > 25 W m^{-2} and wind speeds > 4 m s^{-1}.

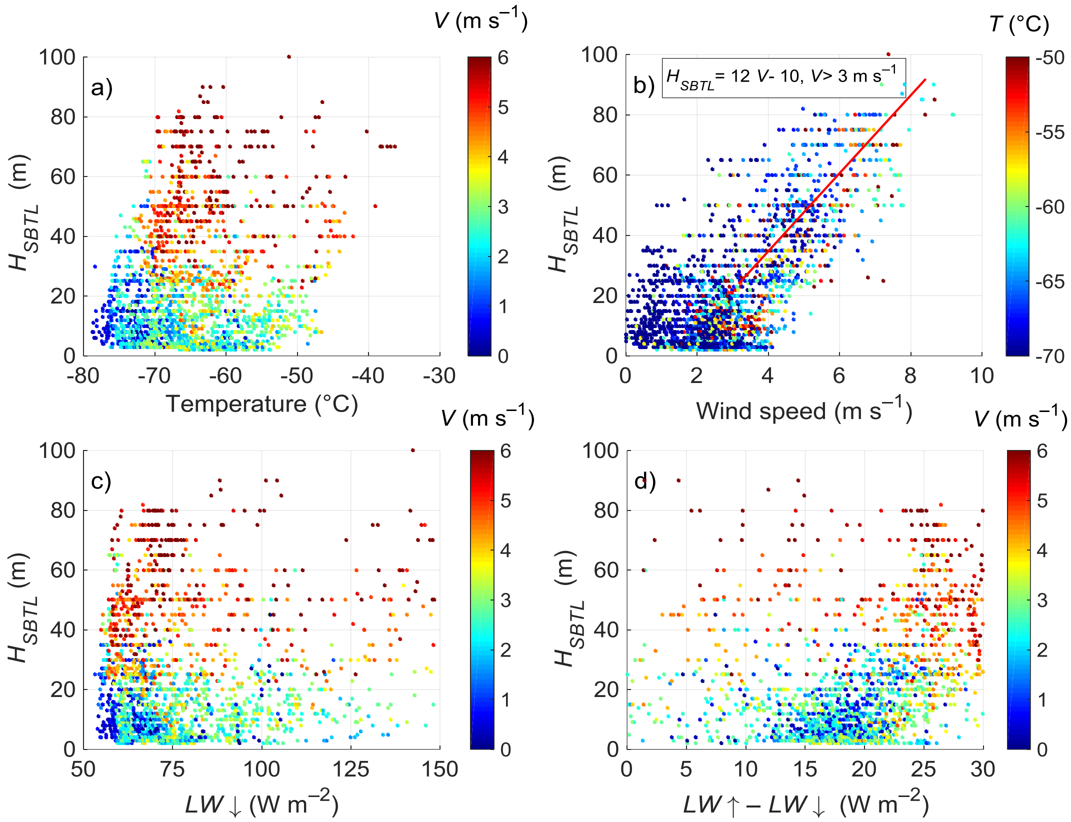

Fig. 7 The depth H_{SBTL} versus **a** temperature at 1.4 m, **b** wind speed at 3.6 m, **c** longwave downwards radiation, **d** the difference between longwave upwards and downwards radiation from April–September 2012

Figure 8a shows H_{SBTL} values versus the difference dT between the temperature at level 2 of the tower (10 m) and the snow-surface temperature T_s, whose dependence can be roughly described by the power law $H_{SBTL} \propto dT^{-\mu_1}$, with a fitted value of the exponent $\mu_1 \approx 1.6$. Figure 8b shows the dependence of H_{SBTL} values on the Brunt–Väisälä frequency N estimated from the temperature gradient between level 2 (10 m) and level 1 (3 m) of the tower, whose dependence is also described by the power law $H_{SBTL} \propto N^{-\mu_2}$ for $\mu_2 \approx 1.4$.

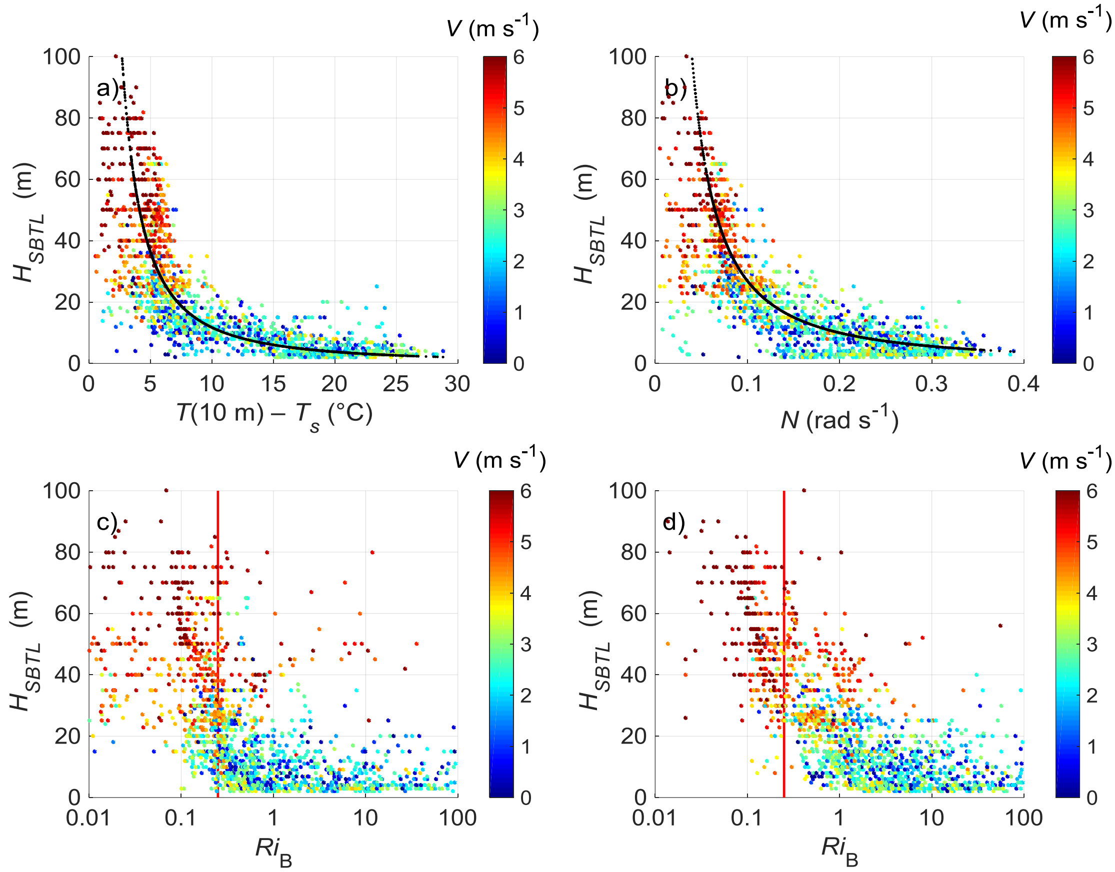

Fig. 8 The depth H_{SBTL} versus the **a** difference between the temperature at 10 m and the snow-surface temperature, **b** Brunt–Väisälä frequency calculated between 10 and 3 m, **c** Richardson number computed between 10 and 3 m, **d** Richardson number computed between 41 and 3 m, from April–September 2012. Black thick lines in **a** and **b** are fitted power-law curves with exponents of −1.6 and −1.4, respectively. Red vertical lines in **c** and **d** show $Ri_B = 0.25$

As for the correlation between the depth H_{SBTL} and the gradient-dependent parameters, examples of vertical profiles of Ri_B and N are shown in Fig. 4e and f, corresponding to the profiles of temperature and wind speed measured and averaged over 2 h between 1900 and 2100 LST on 27 August 2012 (see Fig. 4c and d). The bulk Richardson number Ri_B within the SBTL estimated from temperature and wind-speed gradients on the 45-m tower shows values around and sometimes exceeding 0.25. The persistence of turbulence beyond the critical Richardson number is in agreement with earlier theoretical and experimental results mentioned above. The relationship between H_{SBTL} and Ri_B values is shown in Fig. 8c and d for two Ri_B values calculated with Eq. 3: (i) between the levels z_1= 3 m and z_2= 10 m (Fig. 8c), and (ii) the levels z_1= 3 m and z_2= 41 m (Fig. 8d). It should be noted that the choice of heights to estimate Ri_B values to properly characterize the turbulence behaviour is not a simple task, because the Richardson number Ri_B is quite variable vertically within the SBTL. Therefore, we consider at least two values corresponding to the lowest and highest regions of available measurements. On average, the dependence of H_{SBTL} values on the Richardson number Ri_B shows that a transition between very shallow and deeper SBTL regimes occurs when Ri_B values are in the range between 0.1 and 1, which separates turbulent and very-weak-turbulence conditions. A relatively deep SBTL of 10–20 m may even occur for values $Ri_B > 0.25$. Figure 8c and d shows that there is some difference between the dependence of depth H_{SBTL} on Ri_B values calculated for the different layers [z_1, z_2], which is an ambiguity needing to be taken into account when choosing a proper stability parameter based on the Richardson number Ri_B.

3.2 Description of the Surface-based Turbulent Layer under Synoptically Undisturbed Conditions

While visual inspection of sodar echograms plotted with a conventional scale of the time axis (a few hours on one plot) does not reveal clearly the presence of the internal structure of the SBTL (Figs. 4a, 9a and 11a), plotting the same data with an expanded time scale (for 10–20 min) makes it possible to detect the detailed features of the turbulence structure, which can be either uniformly chaotic (as in Fig. 4b) or quite regular (Fig. 9b$_1$ and b$_2$). As these features often exhibit wavelike behaviour with oscillations of fine-scale turbulent layers (Fig. 9b$_1$ and b$_2$), the difference between different SBTL types consists not only in their depths and the averaged intensity of turbulence, but also in the pattern of the spatial and temporal structure. For classification purposes, data over periods not affected by strong weather changes were selected.

Figure 4a shows an example of the relatively deep SBTL extending up to 40–60 m, and having a uniformly chaotic internal structure without any evident regularity (Fig. 4b). Wind speeds of 3–6 m s^{-1} characterize the meteorological conditions for this situation. Profiles of temperature and wind speed (Figs. 4d and e) show gradients of ≈ 0.05 K m^{-1} and 0.12 s^{-}

^{1}, respectively, which are nearly constant throughout the entire SBTL. Although the value of Ri_B within the SBTL exceeds 0.25 at heights > 20 m, this does not impede the existence of enhanced thermal turbulence. The buoyancy period is ≈ 80 s, but no clear oscillations with this period are detected.

Another kind of relatively deep SBTL (Fig. 9a) is characterized by the presence of wavelike structures propagating downwind and tilted in the direction of motion. A detailed wavy structure of turbulence appears in echograms as a braid (also called herringbone or S-like) waveform clearly visible in the detailed views in Fig. 9b_1 and b_2, illustrating individual braid-like, wavy fine-scale layers of vertical thickness 3–5 m. Such a wave pattern is often referred to as vorticity-generated waves, such as Kelvin–Helmholtz billows (Sun et al. 2015). Another term applied to this wavy pattern is "internal gravity–shear waves" (Ljuljukin et al. 2015) resulting from the shear instability under stable stratification conditions. Wave processes appear mainly as a periodical (8–15 min) passage of wave trains of 4–6 min duration, whose internal structure is evident in Fig. 9b_1 and b_2.

Analysis of the meteorological conditions accompanying these events showed the usual presence of a temperature jump (10–15°C within a thin layer of ≈ 5 m) at heights of 20 to 50 m (as in Fig. 9c), where fine-scale waves occur. The shape of the temperature profile with two inflexion points resembles the one considered earlier by Garratt and Brost (1981), and van Ulden and Holstag (1985). Vignon et al. (2017a) identified the shape of such temperature profiles as "convex–concave–convex". Another necessary attribute of these events is the 3-m wind speed > 4 m s^{-1} with a wind shear of 0.15–0.2 s^{-1} within the SBTL.

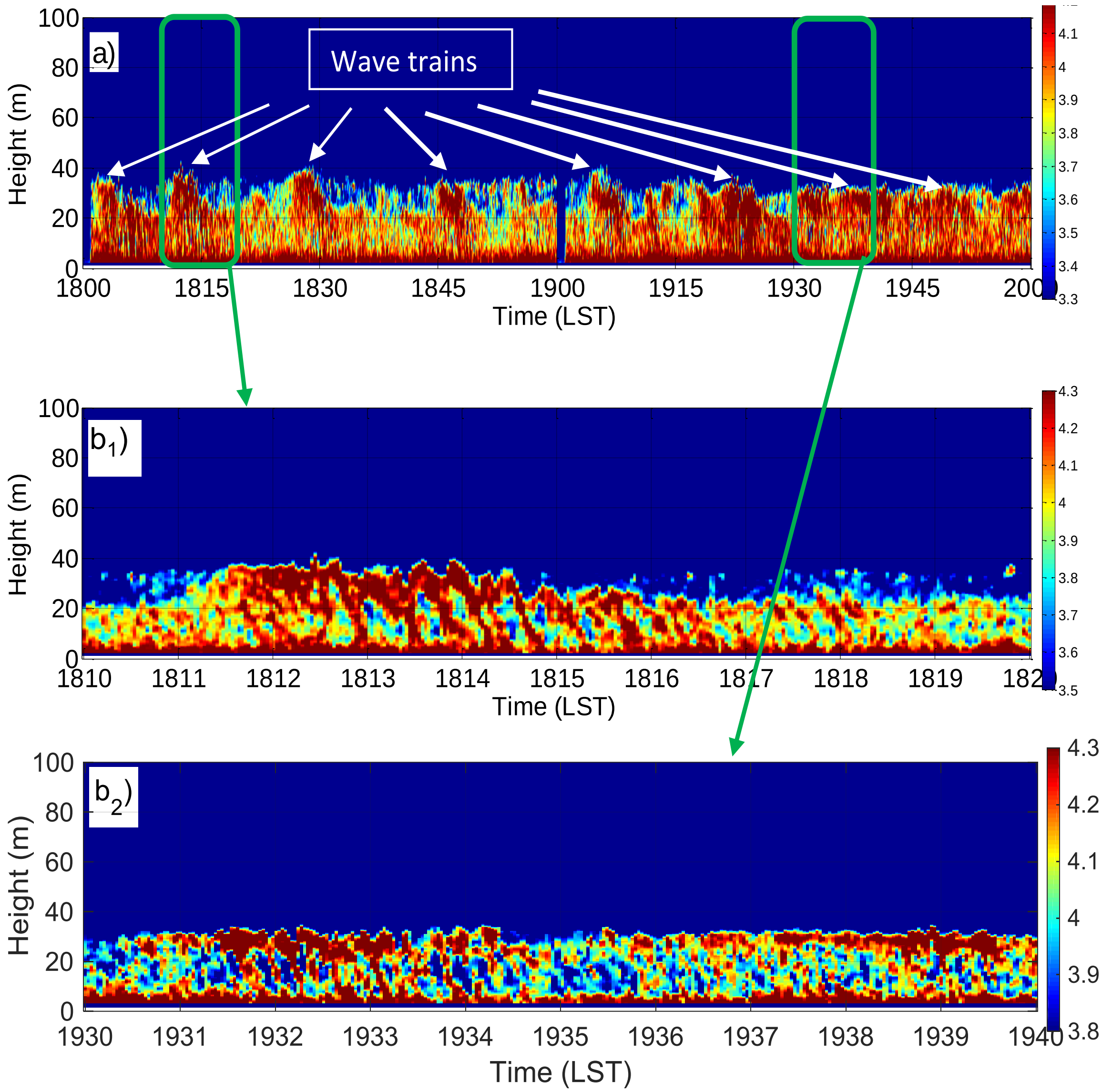
a)
Wave trains
Height (m)
Time (LST)
b$_1$)
Height (m)
Time (LST)
b$_2$)
Height (m)
Time (LST)

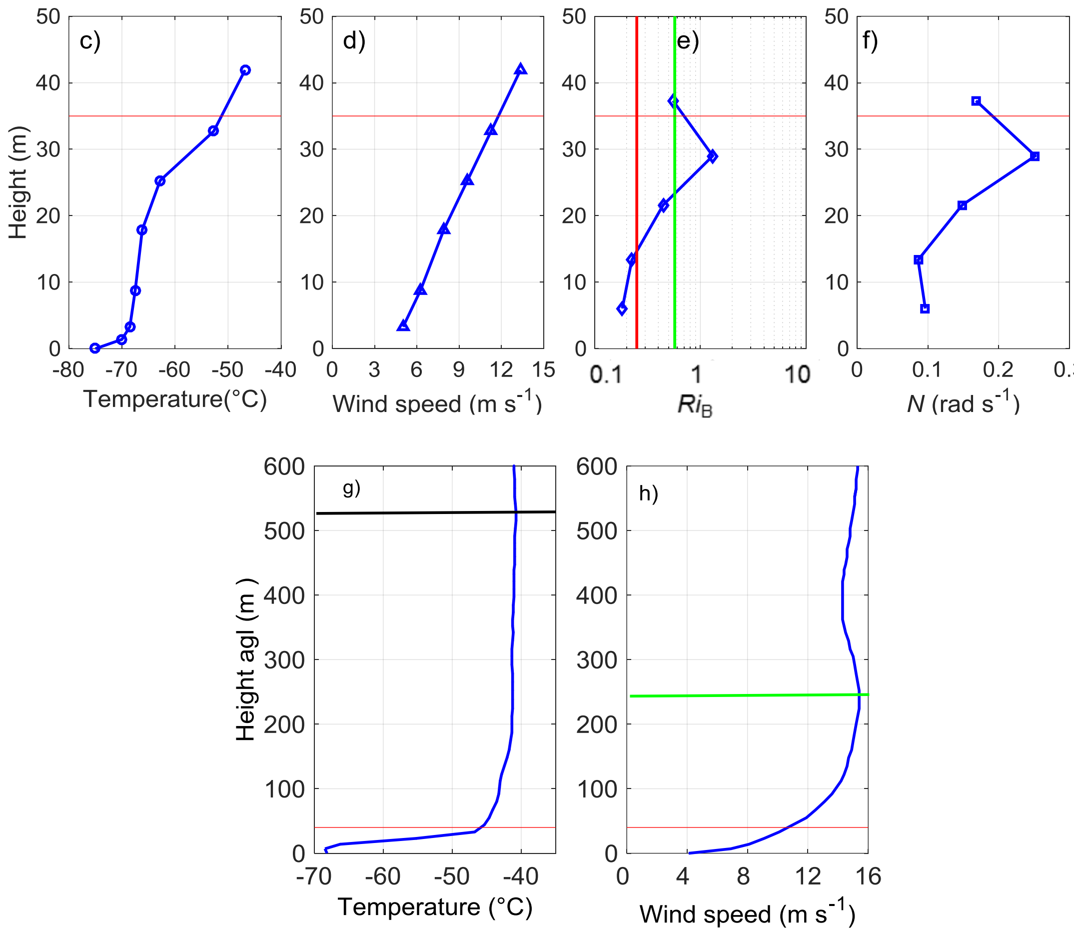

Fig. 9 **a** Example of the long-lived SBTL with a wavy internal structure in the sodar echogram, and recorded on 25 August 2012, 1800–2000 LST. $\mathbf{b_1}$, $\mathbf{b_2}$ Detailed views of the echogram from 1810–1820 LST and 1930–1940 LST showing the internal structure of the wave packets. The colorbars show the logarithm of the structure parameter C_T^2 (arbitrary units). Vertical profiles of **c** temperature, **d** wind speed, **e** Richardson number, and **f** buoyancy frequency averaged over 1900–2000 LST. Vertical profiles of **g** temperature, **h** wind speed measured by a radiosonde on 25 August 2014, 1930 LST. The red vertical line in **e** shows the Richardson number $Ri_B = 0.25$. The green vertical line in **e** shows the value of Ri_B calculated between $z_1 = 3$ m and $z_2 = 41$ m. The thick solid horizontal black line in **g** indicates the position of the top of the temperature inversion layer located at ≈ 530 m. The thick solid horizontal green line in **h** indicates the height of the wind-speed maximum at ≈ 240 m. The horizontal red lines in **c**–**h** indicate the value of H_{SBTL}

Atmospheric waves are an important mechanism for the transport and redistribution of energy, momentum, and matter between the ABL and the free atmosphere, while affecting many micro- and mesoscale processes, such as turbulence, diffusion, local flows, and temperature inversions. For a more accurate estimation of the frequency of the wavelike motions, a spectral analysis was performed, with the spectrum of variations of the structure parameter C_T^2 within the braid region shown in Fig. 10 as a function of both frequency and period. The spectral density was calculated separately for the low-frequency (long periods) and high-frequency (short periods) ranges. The spectral peaks for shorter periods (≈ 20 s) are attributed to the periods of waves shown in Fig. 9b_1 and b_2, which, in many cases, are rather close to the buoyancy period T_b at the layer where waves occur. For the profile in Fig. 9f, the period $T_b \approx 25$ s occurs at a height of ≈ 30 m, as calculated from the frequency N. Unfortunately, layers containing waves are often located above 40 m, so it was not possible to accurately estimate the period T_b. The spectral peak at a long period (≈ 680 s) characterizes the average time interval between successive wave trains, which, for the entire observational period, ranged between 500 and 900 s.

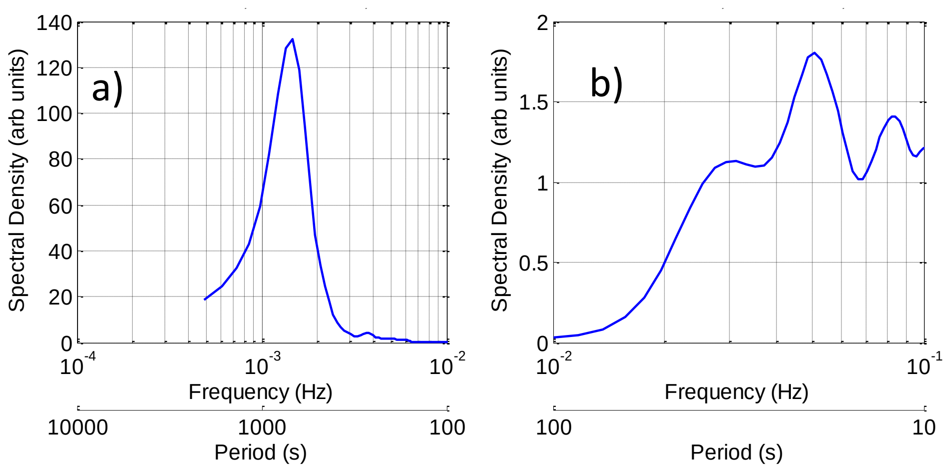

Fig. 10 Low-frequency (**a**) and high-frequency (**b**) parts of the power spectra of the structure parameter C_T^2 within the braid regions from Fig. 8 observed on 25 August 2012 at 1800–2000 LST

While we are aware that single-point measurements are limited in determining the spatial scales of wavelike motions, a rough estimate can be made using Taylor's frozen-turbulence hypothesis, whose applicability for Kelvin–Helmholtz billow-like waves was discussed by Petenko et al. (2016) based on the results reported by Gossard et al. (1970) and Eymard and Weill (1979**)**. For Kelvin–Helmholtz billows (also named as gravity–shear waves), their propagation phase velocity is close to the wind speed and direction. The value of the wavelength λ is estimated as $\lambda = V_l T$, where V_l is the wind speed within the wave layer, and T is the period of waves. This is a tentative step to obtaining information on the spatial characteristics of the wavy pattern. For the observed cases, the values of λ within wave trains are estimated to be 100–200 m, with the horizontal dimension of wavy regions estimated as 2000–3000 m, which is close to the distance separating wave trains (regions without wave activity). As this simple approach provides only a rough estimate, a comprehensive investigation of this phenomenon requires further experiments with multipoint measurements and an advanced theoretical consideration.

Weak turbulence was often observed for depths $H_{SBTL} < 15$ m (Fig. 11a), which are very shallow layers occurring ≈ 50 % of the time. The meteorological conditions leading to reduced turbulence are characterized by low wind speeds < 3 m s^{-1} and temperatures < −70°C. Temperature profiles show very strong gradients near the surface, with a difference sometimes exceeding 20°C in the first 20 m, and a shape resembling an "exponential" profile (see, e.g., van Ulden and Holstag 1985; Vignon et al. 2017a). The wind speed increases from 0–3 m s^{-1} at 3 m, reaching local maxima of 3–5 m s^{-1} at 20–100 m.

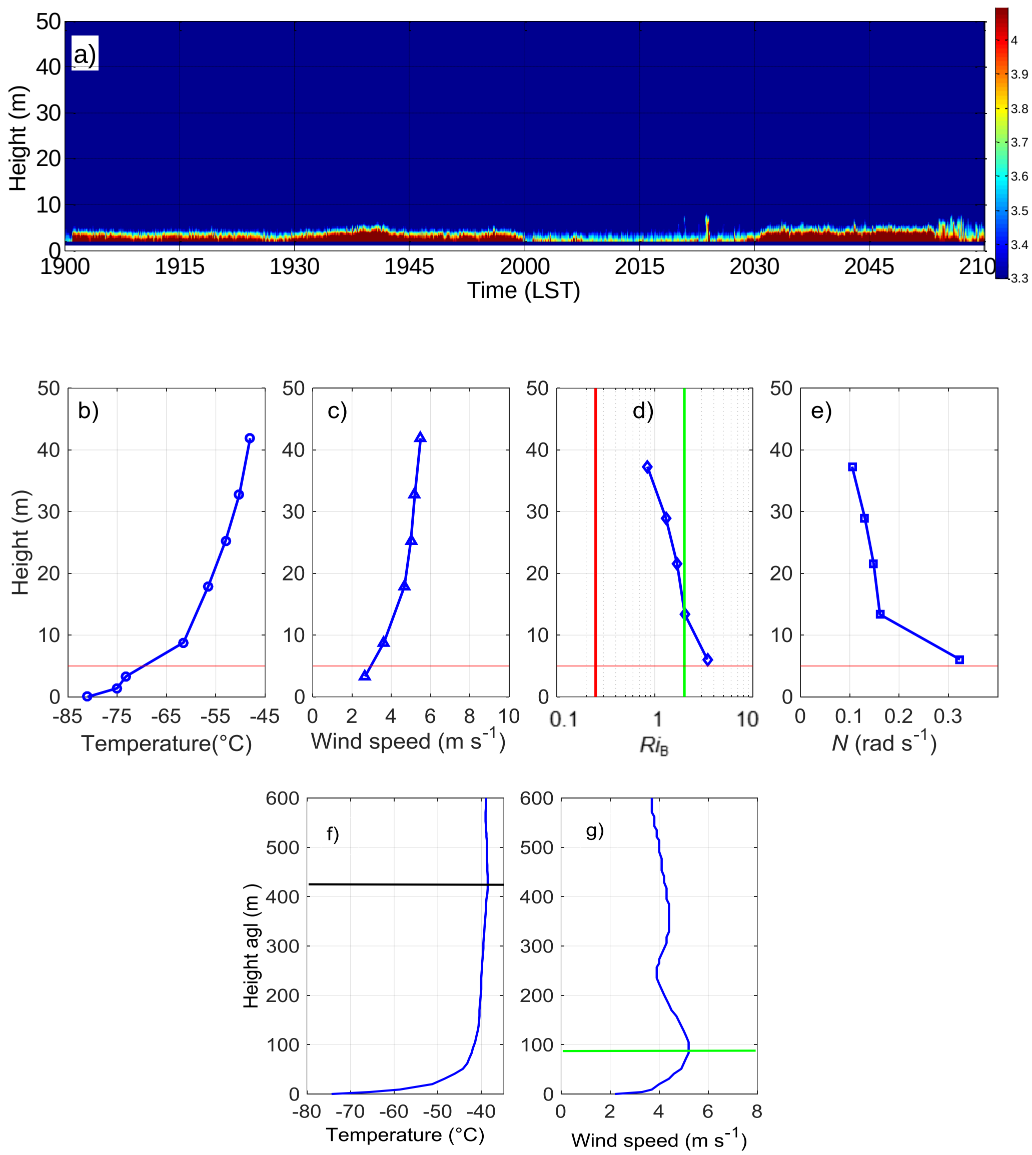

Fig. 11 Example of the very shallow layer H_{SBTL} < 5 m observed on 31 August 2012; the colorbar shows the logarithm of the structure parameter C_T^2 (arbitrary units). Vertical profiles of **b** temperature, **c** wind speed, **d** Richardson number, and **e** Brunt–Väisälä frequency measured on 31 August 2012, 1900–2100 LST. The solid horizontal red lines in **b**–**e** indicate the position of the top of the turbulent layer located at 5 m. The thick solid horizontal black line in **f** indicates the position of the top of the temperature inversion layer located at ≈ 420 m. The thick solid horizontal green line in **g** indicates the height of the wind-speed maximum at ≈ 90 m

Elevated turbulent layers at heights > 15 m were occasionally (≈ 8%) observed above the very shallow SBTL (Fig. 12), including both sporadic and long-term, non-regular, as well as wavelike, elevated turbulent layers.

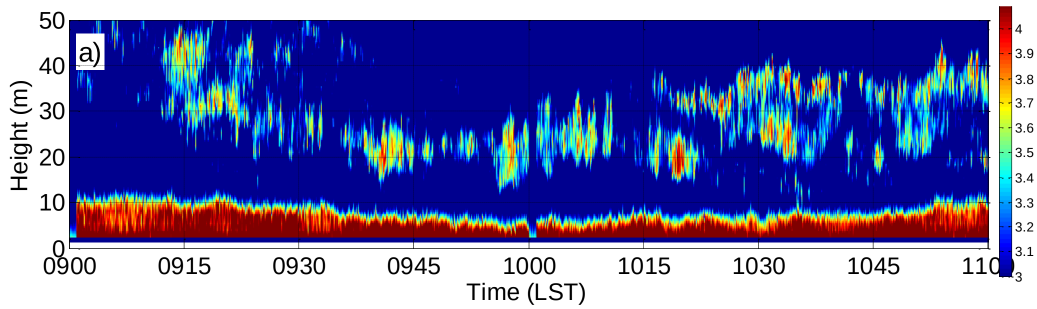

Fig. 12 Example of the very shallow SBTL accompanied with an elevated turbulent layer observed on 28 May 2012; the colorbar shows the logarithm of the structure parameter C_T^2 (arbitrary units)

Table 2. Meteorological parameters for different SBTL types,

Type	V at 3.6 m (m s^{-1})	T at 1.4 m (°C)	$T_{1.4m} - T_s$ (°C)	Temperature profile shape	Occurrence %
Very shallow H_{SBTL} < 15 m	0–4	−80 to −60	3–10	exponential	50
Shallow, uniform H_{SBTL} ≈ 15–70 m	1–6	−70 to −50	3–7	Convex–concave–convex	23
Shallow, wavy H_{SBTL} ≈ 20–70 m	4–8	−70 to −50	2–7	Convex–concave–convex	21

Based on the above description of the observed properties of the SBTL, we suggest an approximate categorization of SBTL types, taking into account both the depth and internal structure, and considering periods without any significant weather changes. Roughly, we distinguish situations with reduced and enhanced turbulence, resulting in the following types:

1) very shallow layer of depth < 15 m (Fig. 11a) sometimes accompanied with thin elevated sub-layers at 20–50 m (Fig. 12);

2) shallow of depth 15–70 m with uniformly chaotic internal structure (Fig. 4);

3) shallow of depth 20–70 m with wavy internal structure (Fig. 9).

While we define three principal types, this number represents a very subjective oversimplification. These types occur at certain values and gradients of *V* and *T*, but the ranges of *V* and *T* for different types are not well distinguished, and intersect at the rough limits for each type given in Table 2. Multiple values of temperature gradients for a given value of *V* under different turbulent regimes were observed by Vignon et al. (2017a), who suggested that the SBL may evolve like a two-regime dynamical system, with a critical transition, and associated with hysteresis. Histograms in Fig. 13 provide additional information about the probability distribution of the wind speed and the temperature gradient near the surface for each SBTL type. The very shallow SBTL is observed under the lowest wind speeds < 4 m s^{-1}, showing very weak turbulence activity. The deeper SBTL of depth > 15 m and a uniform structure is observed under the wider range of wind speeds 2–7 m s^{-1}, while the SBTL with waves mainly occurs for the higher wind speeds 4–8 m s^{-1}. The highest temperature differences favour the existence of the very shallow SBTL, with the second and third types appearing for the same near-surface temperature gradients. However, an important difference between the uniform and the wavy SBTL is the shape of temperature profiles: within wavy layers, profiles of the pronounced "convex–concave–convex" shape are observed showing the maximum gradient of 0.1–0.2 K m^{-1} in the upper part of the layer.

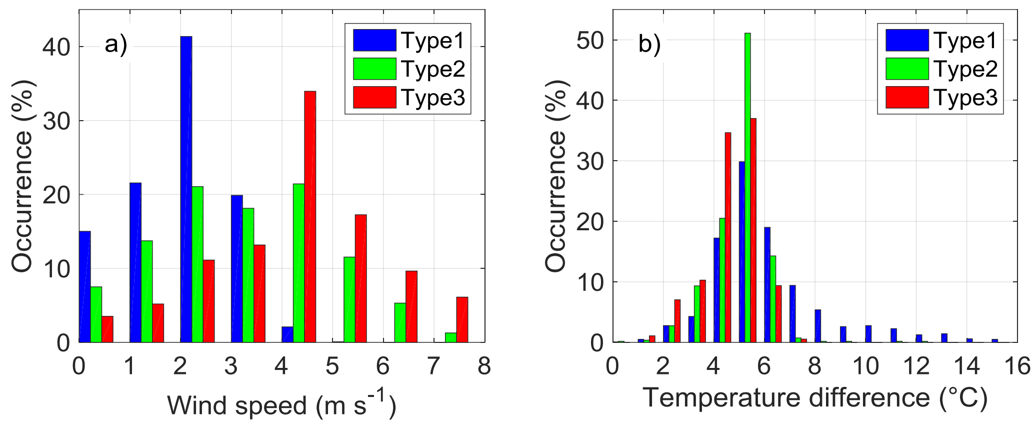

Fig. 13 Histograms of **a** wind speed at 3.6 m, and **b** temperature difference (between 1.4 m and the snow surface) for different SBTL types

To emphasize the importance of the shape of temperature profiles in characterizing the different types, Fig. 14 shows "spaghetti" profiles of the difference between the temperatures at heights z (seven levels from the automatic weather station and the tower) and the snow-surface temperature, which are plotted versus height normalized by the depth H_{SBTL}. Separate plots are shown for all three types, and profiles are shown separately for the two wind-speed ranges: 1) $V < 2$ m s^{-1} (red lines) and $V > 2$ m s^{-1} (green lines) for type 1; 2) $V < 4$ m s^{-1} (red lines) and $V > 4$ m s^{-1} (green lines) for types 2 and 3, respectively.

Temperature profiles observed for type 1 have a clear exponential shape (Fig. 14a), reflecting the logarithmic dependence on height $T(z/H_{SBTL}) \propto \ln(z/H_{SBTL})$. The uniform (type 2) and the wavy (type 3) types do not differ essentially in the shape of their temperature profiles; profiles of a pronounced "convex–concave–convex" shape with two inflexion points are observed showing the maximum gradient of 0.2–2 K m^{-1} (0.2–1 K m^{-1} for type 2 and 1–2 K m^{-1} for type 3) in the upper part of the SBTL. The main difference is the higher temperature gradients around the second inflexion point when waves occur. Average gradients for normalized profiles from Fig. 14b and c are ≈ 14 K for type 2 and ≈ 32 K for type 3. Changes in the curvature of temperature profiles at Dome C were observed earlier by Genthon et al. (2013) and Vignon et al. (2017a), with the latter attributing these changes to the different SBL regimes.

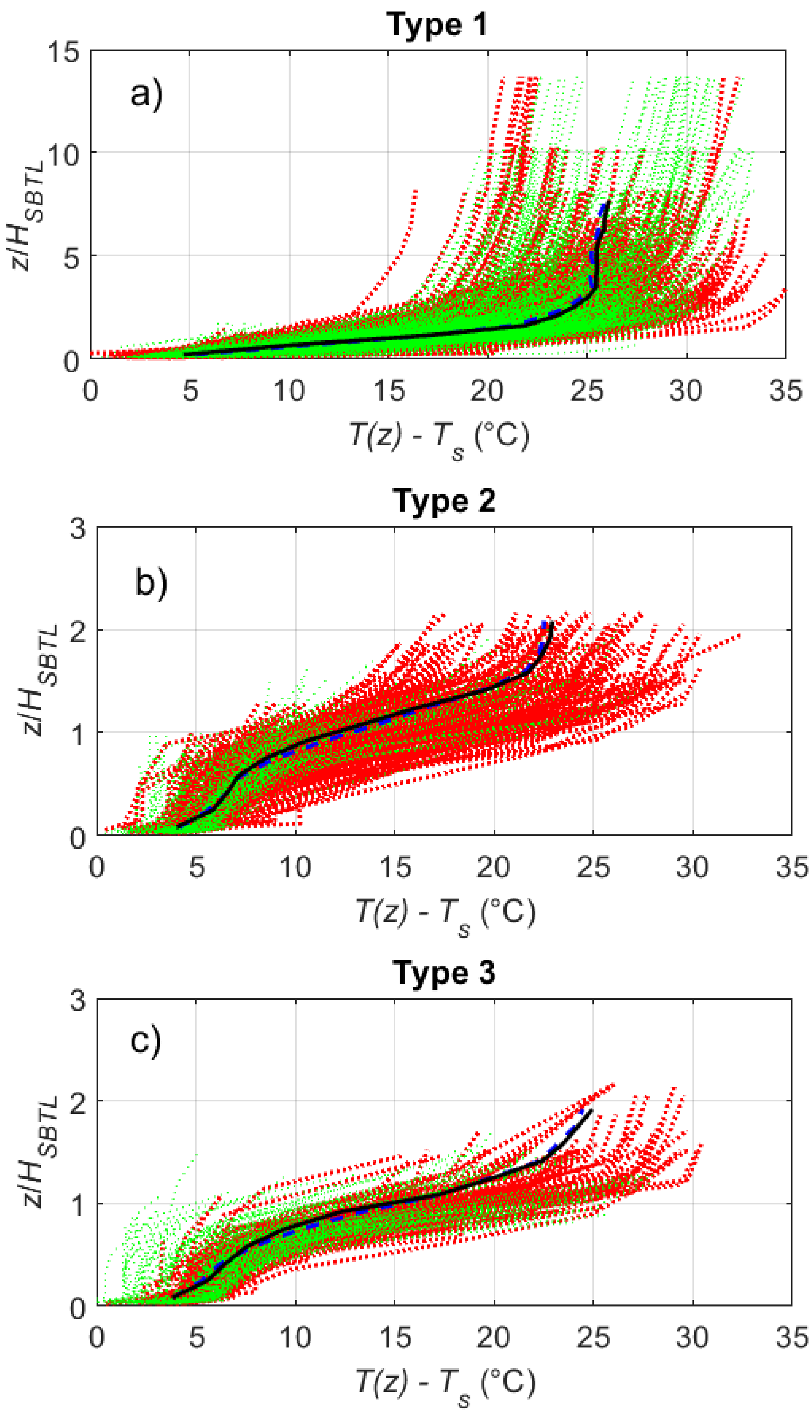

Fig. 14 "Spaghetti" plots of temperature profiles for different SBTL types. **a** Very shallow with depths $H_{SBTL} < 15$ m; **b** shallow, uniform with depths $H_{SBTL} \approx 15$–70 m; **c** shallow, wavy with depths $H_{SBTL} \approx 20$–70 m. The red and green lines denote wind speeds $V < 4$ m s^{-1} and $V > 4$ m s^{-1}, respectively. The thick solid black lines show median profiles; the thick dashed blue lines show mean profiles

3.3 Examples of Episodic Wavelike Mesoscale Phenomena under Synoptic Changes

The above-mentioned classification is only valid for steady fair-weather conditions. Here, we will discuss periods of significant weather changes caused by the passage of fronts, when the structure of the ABL shows various spatial and temporal patterns. During synoptic changes accompanied with variations in wind speed and direction, temperature, pressure, as well as the appearance of cloudiness, various sub-mesoscale phenomena were observed: 1) solitary waves (single or grouped in 2–5 waves) of duration ≈ 5 min and height ≈ 100 m, 2) steady, sporadic or wavy elevated layers at heights of > 50 m. Examples of these events are shown in Figs. 15 and 16.

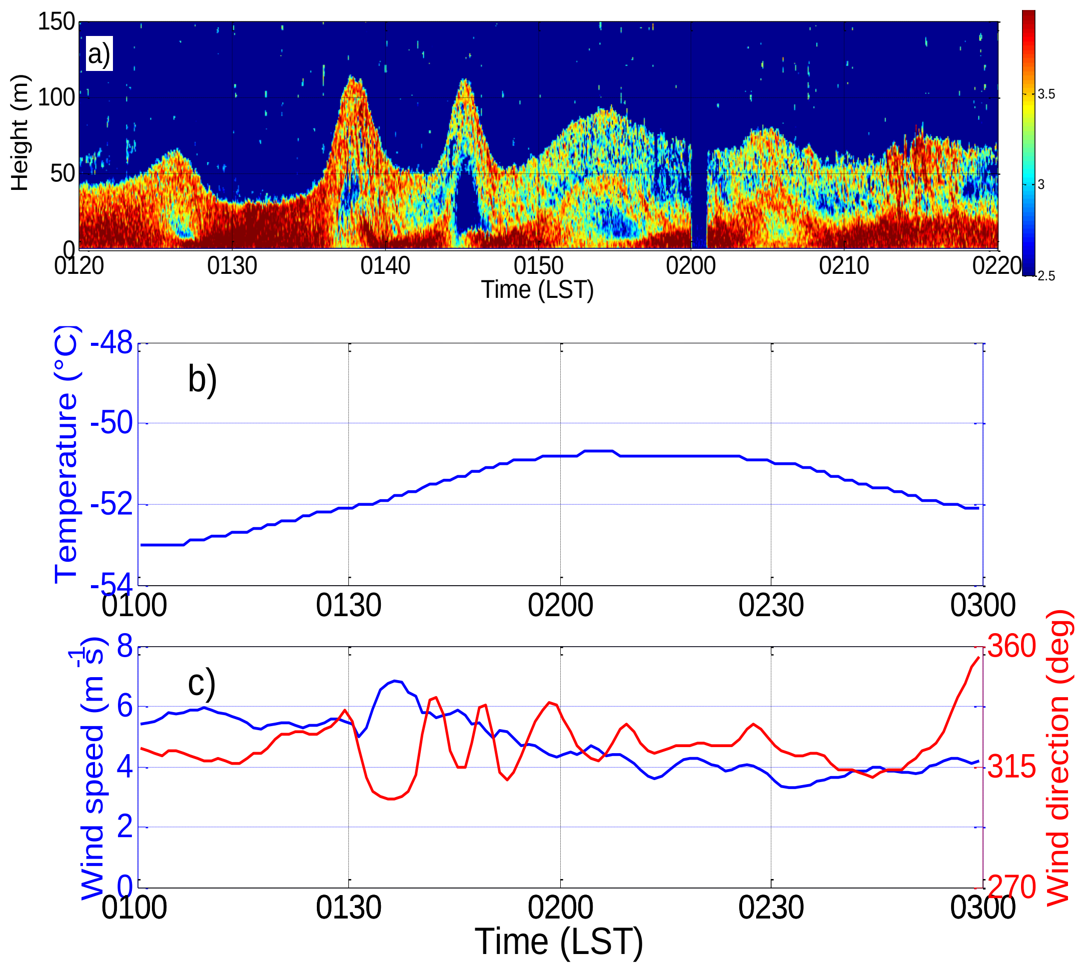

Fig. 15 Passage of a solitary wave packet on 22 July 2012. **a** Sodar echogram showing the wavelike structure; the colorbar shows the logarithm of the structure parameter C_T^2 (arbitrary units). Time variations of **b** 1.4-m temperature and **c** 3.6-m wind speed and direction recorded by the automatic weather station

Figure 15 shows the passage of a packet of solitary waves, indicating periods between solitons varying from 8 to 11 min, and the total number of propagating solitons of six. This event was accompanied with an increase in temperature of ≈ 2°C and oscillations in wind direction and speed. A case study of turbulence generated by a solitary wave is given by Sun et al. (2004). A similar pattern, but in oceanic waves, was observed by Alpers et al. (2008) in the Mediterranean Sea north of the Strait of Messina.

Figure 16 shows the passage of a packet of internal buoyancy waves during a cold-front passage accompanied by the reduction in temperature by 2°C h^{-1}, a step change in wind speed from 2 m s^{-1} to 4 m s^{-1}, and wind veering from 45° to 165°. This phenomenon is characterized by the presence of two wavy turbulent layers: 1) the surface-based layer with an oscillating upper boundary of 5–10 m, and 2) the wavy turbulent layer of variable magnitude, whose crest-to-crest amplitude varies from 60 to 140 m, with the upper boundary changing from 80 to 170 m; the period of oscillations is ≈ 3 min, and the corresponding angular frequency is 0.035 rad s^{-1}; both layers oscillated in phase.

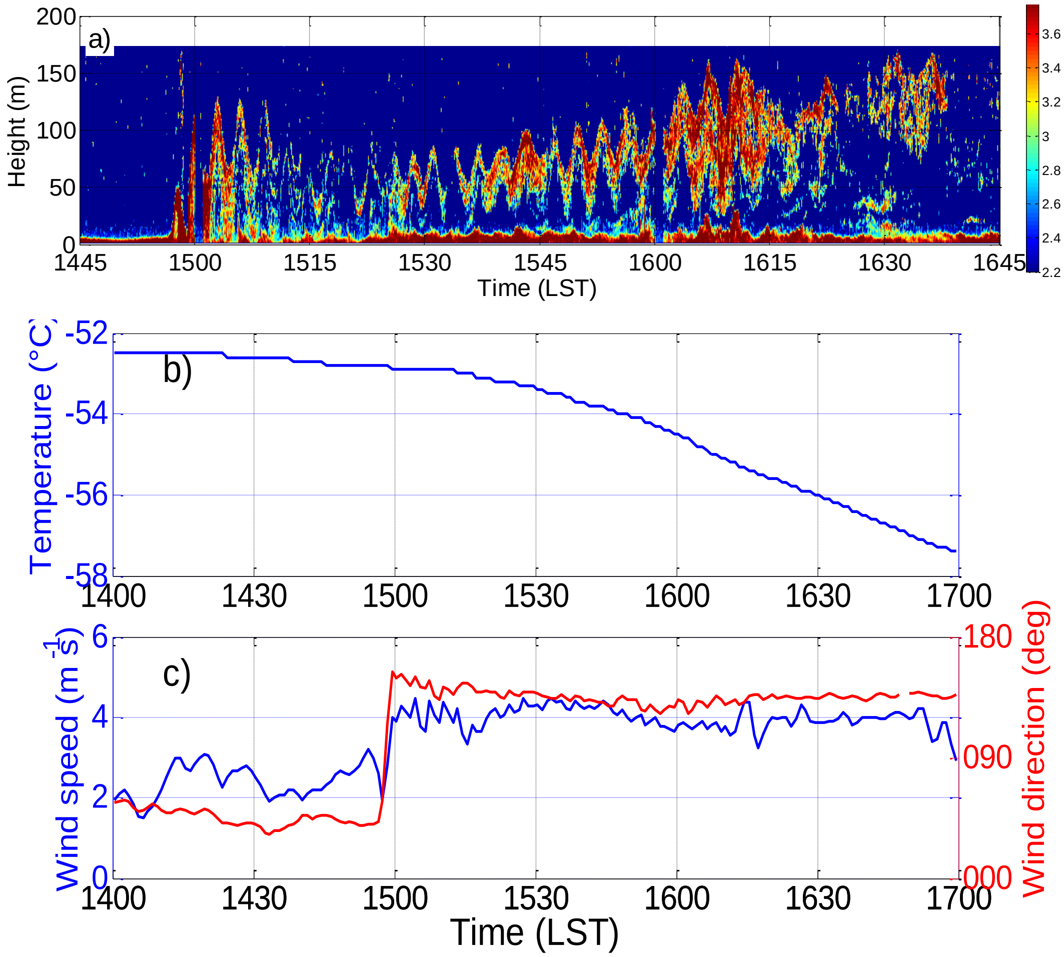

Fig. 16 Propagation of a packet of internal buoyancy waves during a cold-front passage on 25 August 2012. **a** Sodar echogram showing the ABL structure; the colorbar shows the logarithm of the structure parameter C_T^2 (arbitrary units). Time variations of **b** temperature at 1.4 m and **c** wind speed and direction at 3.6 m recorded by the automatic weather station

4 Summary

Our data provide information on the features of turbulence in the ABL on the high Antarctic plateau (Dome C) in very strong static stability at extremely low temperatures in winter, making them useful for the verification of numerical models aiming to resolve such turbulence. Significant thermal turbulence often occurs and extends up to several tens of metres in spite of (i) the large static stability due to strong temperature inversions extending up to 100–600 m, with a total inversion strength reaching 20–40°C at very low temperatures, (ii) the absence of orographic features, and (iii) the absence of the diurnal cycle of solar heating. The advanced high-resolution sodar has made possible the visualization of the fine-scale structure of the SBTL in hitherto unavailable detail, including direct experimental determination of the SBTL depth at Dome C during the whole winter for the first time. Specific features of the spatial and temporal behaviour of thermal turbulence were determined and analyzed, with such turbulence found to be quite vivid and lively, showing different and changeable intermittent patterns in the SBTL. The spatial and temporal distribution of turbulence in winter is more complicated, and exhibits a larger variety of forms than in the summer.

It is necessary to clearly distinguish between the whole SBL and the surface-based *turbulent* layer, which, consistent with previous results, can differ in depth. In our measurements at Dome C, the significant and persistent depths $H_{INV} >> H_{SBTL}$ (more than one order of magnitude) were observed for the first time. The SBTL varies between a few to several tens of metres with an average depth of ≈ 23 m, and occupies only the lowest 3–15% of the temperature inversion layer of average height ≈ 380 m. Also, it was revealed that the magnitude of H_{SBTL} at Dome C is markedly less than the height of the wind-speed maximum H_{Vmax}.

That the SBTL depth increases with the wind speed is perhaps the key factor influencing the intensity and structure of turbulence in the lowermost polar atmosphere. For the wind speed at 3 m, $V > 3$ m s^{-1}, and the relationship between the parameters H_{SBTL} and V can be roughly estimated as $H_{SBTL} \approx 12V - 10$. Another parameter that seems to influence the magnitude of H_{SBTL} is the temperature gradient near the surface. The dependence of the SBTL depth on the frequency N calculated between 10 and 3 m is well described by a power law with an exponent of about −1.4. No simple relationship between the depth H_{SBTL} and either the air-temperature or radiation characteristics is observed.

As for the relationship between the parameters H_{SBTL} and Ri_B, it is difficult to determine any fixed Ri_B value separating conditions for turbulent and very-weak-turbulence regimes. In the Richardson number range $0.2 < Ri_B < 1$, the depths $5 < H_{SBTL} < 60$ m can occur, and the transition range depends on how the Richardson number Ri_B is determined. The "convex–concave–convex" shape of temperature profiles with inflexion points varying with depth H_{SBTL} makes it difficult to unambiguously define the representative value of Ri_B.

Visual inspection of more than 2500 h of sodar records helped classify the SBTL for synoptically undisturbed conditions into several types, since it should be characterized not only by its depth and intensity, but also by its internal structure. We observe three different SBTL types in the periods without considerable weather changes, but emphasize this is a very subjective oversimplification based on typical vertical profiles of temperature, wind speed, Richardson number and Brunt–Väisälä frequency:

1) very shallow depth $H_{SBTL} < 15$ m without any visible regularity of the internal structure (sometimes with sporadic elevated bursts and sublayers);

2) shallow depth $H_{SBTL} = 15–70$ m with a uniform internal structure without any visible regularity;

3) shallow depth $H_{SBTL} = 20–70$ m with a wavy internal structure showing the braid-like fine-scale structures lasting several hours. The characteristic temporal and spatial scales of waves were estimated.

For type 1, temperature profiles show a logarithmic dependence on height having a clear convex exponential shape. Both the uniform and the wavy types 2 and 3, which do not differ essentially in their shapes of temperature profiles, have 'convex–concave–convex' profiles with two inflexion points, and maximum gradients in the upper part of the layer. Moreover, in regions with enhanced turbulence, the Richardson number varies considerably around, and sometimes markedly exceeding, a value of 0.25, in agreement with the theoretical predictions and observations of others. In comparison with the two-regime classification proposed in recent studies, our grouping of the SBTL into three types assumes additionally that, in reality, for a regime of continuous turbulence (or, in other terms, weakly stable one), there are two different SBTL types according to whether the internal structure of turbulence is modulated by wave motions or not.

Additionally, during weather changes, other clearly organized sub-mesoscale events were observed: (i) solitary waves (single or grouped in 2–5 solitons) with duration of ≈ 5–10 min each, and height of ≈ 50–100 m, and (ii) internal buoyancy waves with variable amplitudes of 50–150 m and periods of 3–4 min.

The use of the high-resolution sodar enables clear visualization of the most striking features in the SBTL, indicating the frequent presence (> 20 %) of wavelike phenomena of periods from a few tens of seconds to several minutes, which are of particular interest for the more realistic representation of the SBL. A variety of wavy structures with periods of oscillations from 20 s to a few minutes are often evident in the sodar records, with the vertical amplitude of the oscillations varying from a few metres to a few of tens of metres. Waves were observed under stationary weather conditions, but especially during synoptic perturbation episodes during the intrusion of coastal air masses. Therefore, the challenging problem in atmospheric physics concerning the vertical transfer from the near surface to the overlying atmosphere under very stable stratification is unlikely to be resolved without the consideration of wave processes. Often, regular and wavy fine-scale layers forming a braid pattern associated with internal gravity–shear waves at periods of 20–50 s are observed within periodical (of 8–15 min) wave trains of durations of 4–6 min and containing 10–20 wave crests. The periods of these fine-scale waves are close to the buoyancy periods T_b estimated from the temperature gradients in the layer where waves occur. Wavelengths within wave trains are estimated to be of magnitudes 100–200 m. The entire depth of the turbulent layer containing waves varies from 20 to 70 m. The appearance of these wave structures is accompanied by very sharp temperature changes (8–12°C through 7 m) at heights of 20–40 m, and wind speeds of 4–8 m s^{-1}. Mechanisms of the generation of this kind of wave activity are of special interest.

We provide an approximate overview of the features of the SBTL structure at the Antarctic plateau during the winter period, and believe a high-resolution sodar is an important auxiliary instrument in investigations of the SBL for the proper interpretation of accurate in situ measurements of both mean and turbulent atmospheric parameters. Results from 2012 argue for more comprehensive studies based on long-term sodar and micro-meteorological observations carried out during 2012, 2014 and 2015, as well as for further experimental campaigns.

Acknowledgements We thank the Italian National Programme of Researches in Antarctica (PNRA) and the Paul-Emile Victor French Polar Institute (IPEV) running the Concordia station for making possible a study in this special place. This research has been done in the framework of the projects “Mass lost in wind flux” (MALOX), and “Concordia multi-process atmospheric studies” (COMPASS) sponsored by the PNRA. A special thanks to P. Grigioni and all the stuff of the Antarctic Meteo-Climatological Observatory at Concordia of the PNRA for providing the data and information from the automatic weather station and radiosoundings obtained from the IPEV/PNRA Project “Routine Meteorological Observations at Station Concordia” (http://www.climantartide.it). M. Kallistratova acknowledges the grant of the Russian Foundation for Basic Research, Project No 16-05-01072. The authors are also thankful to G. Mastrantonio, A. Viola, and A. Conidi for their assistance in preparing the experimental equipment, and to the logistics staff of the Concordia station for their help during the field work. We would like to thank three anonymous reviewers for their careful reading of our manuscript and many insightful comments and constructive suggestions. The authors are thankful to B. van de Wiel, A. Grachev, V. Gryanik, R. Sozzi, E. Vignon, and S. Zilitinkevich for useful discussions and comments.

References

Alpers W, Brandt P, Rubino A (2008) Internal waves generated in the Straits of Gibraltar and Messina: observations from space. In: Barale V, Gade M (eds) Remote Sensing of the European Seas. Springer, Dordrecht, pp 319-330. doi:10.1007/978-1-4020-6772-3_24

André JC, Mahrt L (1982) The nocturnal surface inversion and influence of clear-air radiative cooling. J Atmos Sci 39:864-878

Argentini S, Petenko I, Mastrantonio G, Bezverkhnii V, Viola A (2001) Spectral characteristics of East Antarctica meteorological parameters during 1994. J Geophys Res 106:12463-12476

Argentini S, Mastrantonio G, Petenko I, Pietroni I, Viola A (2012) Use of a high-resolution sodar to study surface-layer turbulence at night. Boundary-Layer Meteorol 143:177-188

Argentini S, Pietroni I, Mastrantonio G, Viola A, Dargaud G, Petenko I (2014a) Observations of near surface wind speed, temperature and radiative budget at Dome C, Antarctic Plateau during 2005. Antarctic Sci 26(1):104-112. doi:10.1017/S0954102013000382

Argentini S, Petenko I, Pietroni I, Viola A, Mastrantonio G, Casasanta G, Aristidi E, Ghenton C (2014b) The surface layer observed by a high resolution sodar at Dome C, Antarctica. Annals Geophys 56(5), 10.4401/ag-6347

Baas P, Steeneveld GJ, van de Wiel BJH, Holtslag AAM (2006) Exploring self-correlation in flux-gradient relationships for stably stratified conditions. J Atmos Sci 63(11):3045—3054

Banta RM, Newsom RK, Lundquist JK, Pichugina YL, Coulter RL, Mahrt L (2002) Nocturnal low-level jet characteristics over Kansas during CASES-99. Boundary-Layer Meteorol 105:221-252

Banta RM (2008) Stable-boundary-layer regimes from the perspective of the low-level jet. Acta Geophysica 56:58-87

Beyrich F (1997) Mixing height estimation from sodar data—a critical discussion. Atmos Environ 31(23):3941–3953

Bretherton FP (1969) Waves and turbulence in stably stratified fluids. Radio Sci 4(12):1279-1287

Brown EH, Hall Jr FF (1978) Advances in atmospheric acoustics. Rev Geophys 16:47–110

Brun E, Six D, Picard G, Vionnet V, Arnaud L, Bazile E, Boone A, Bouchard A, Genthon C, Guidars V, Le Moigne P, Rabier F, Seity Y (2011) Snow/atmosphere coupled simulation at Dome C, Antarctica. J Glaciol 52:721–736. doi:10.3189/002214311797409794

Casasanta G, Pietroni I, Petenko I, Argentini S (2014) Observed and modelled mixing layer height at Dome C, Antarctica. Part I: the convective boundary layer. Boundary-Layer Meteorol 151:597-608. doi:10.1007/s10546-014-9907-5

Drüe C, Heinemann G (2007) Characteristics of intermittent turbulence in the upper stable layer over Greenland. Boundary-Layer Meteorol 124:361-381. doi:10.1007/s10546-007-9175-8

Emmanuel CB, Bean BR, McAllister LU, Pollard JR (1972) Observation of Helmholtz waves in the lower atmosphere with an acoustic sounder. J Atmos Sci 29:886-892

Eymard L, Weill A (1979) A study of gravity waves in the planetary boundary layer by acoustic sounding. Boundary-Layer Meteorol 17:231-245

Galperin B, Sukoriansky S, Anderson PS (2007) On the critical Richardson number in stably stratified turbulence. Atmos Sci Lett 8:65–69

Garratt JR and Brost RA (1981) Radiative cooling within and above the nocturnal boundary layer. J Atmos Sci 38:2730–2746

Genthon C, Gall´ee H, Six D, Grigioni P, Pellegrini A (2013) Two years of atmospheric boundary layer observations on a 45-m tower at Dome C on the Antarctic plateau. J Geophys Res Atmos 118:3218-3232. doi:10.1002/jgrd.50128

Gossard EE, Richter JH, Atlas D (1970) Internal waves in the atmosphere from high-resolution radar measurements. J Geophys Res Oceans Atmos 75:3523-3536. doi:10.1029/JC075i018p03523

Gossard EE, Gaynor JE, Zamora RJ, Neff WD (1985) Fine structure of elevated stable 1ayers observed by sounder and in situ tower sensors. J Atmos Sci 42:21562169

Grachev AA, Fairall CW, Persson POG, Andreas EL, Guest PS (2005) Stable boundary layer scaling regimes: The SHEBA data. Boundary-Layer Meteorol 116:201-235

Grachev AA, Andreas EL, Fairall CW, Guest PS, Persson POG (2013) The critical Richardson number and limits of applicability of local similarity theory in the stable boundary layer. Boundary-Layer Meteorol 147:51-82. doi:10.1007/s10546-012-9771-0

Gur'yanov AE, Kallistratova MA, Kutyrev AS, Petenko IV, Scheglov PV, Tokovinin AA (1992) The contribution of the lower atmospheric layers to the seeing at some mountain observatories. Astron Astrophys 262:373-381

Holtslag AAM, Nieuwstadt FTM (1986) Scaling the atmospheric boundary layer. Boundary-Layer Meteorol 36:201-209

Hooke WH, Hall FF Jr, Gossard EE (1973) Observed generation of an atinospheric gravity wave by shear instability in the mean flow of the planetary boundary layer. Boundary-Layer Meteorol 5:29-41

Howard L (1961) Note on a paper of John W. Miles. J Fluid Mech 10:509–512

Joffre SM, Kangas M, Heikinheimo M, Kitaigorodskii SA (2001) Variability of the stable and unstable atmospheric boundary-layer height and its scales over a boreal forest. Boundary-Layer Meteorol 99(3):429-450. https://doi.org/10.1023/A:10189565

Kallistratova MA, Petenko IV (1993) Aspect sensitivity of sound backscattering in the atmospheric boundary layer. Appl Phys B 57:41-48

King JC, Mobbs SD, Darby MS, Rees JM (1987) Observations of an internal gravity wave in the lower troposphere at Halley, Antarctica. Boundary-Layer Meteorol 39:1-13

Kitaigorodskii SA, Joffre SM (1988) In search of a simple scaling for the height of the stratified atmospheric boundary layer. Tellus 40A:419-433. doi:10.1111/j.1600-0870.1988.tb00359.x

Klipp CL, Mahrt L (2004) Flux–gradient relationship, self-correlation and intermittency in the stable boundary layer. Q J R Meteorol Soc 130(601):2087–2103

Kouznetsov RD (2009) The summertime ABL structure over an Antarctic oasis with a vertical Doppler sodar. Meteorol Z 18:163-167

Lyulyukin VS, Kallistratova MA, Kouznetsov RD, Kuznetsov DD, Chunchuzov IP, Chirokova GYu (2015) Internal gravity-shear waves in the atmospheric boundary layer by the acoustic remote sensing data. Izv Atmos Oceanic Phys 51(2):193-202

Mahrt L (1999) Stratified atmospheric boundary layers. Boundary-Layer Meteorol 90:375-396

Mahrt L (2010) Variability and maintenance of turbulence in the very stable boundary layer. Boundary-Layer Meteorol 135:1-18

Mahrt L (2014) Stably stratified atmospheric boundary layers. Ann Rev Fluid Mech 46:23-45

Mahrt L, Richardson S, Seaman N, Stauffer D (2012) Turbulence in the nocturnal boundary layer with light and variable winds. Q J R Meteorol Soc 138:1430-1439

Mahrt L, Sun J, Blumen W, Delaney T, Oncley S (1998) Nocturnal boundary layer regimes. Boundary-Layer Meteorol 88:255-278

Mahrt L, Vickers D (2006) Extremely weak mixing in stable conditions. Boundary-Layer Meteorol 119:19-39

Melgarejo JW, Deardorff JW (1974) Stability functions for the boundary layer resistance laws based upon observed boundary layer heights. J Atmos Sci 31:1324–1333

Miles JW (1961) On the stability of heterogeneous shear flows. J Fluid Mech 10:496508.

Mironov D, Fedorovich E (2010) On the limiting effect of the Earth's rotation on the depth of a stably stratified boundary layer. Q J R Meteorol Soc 136:1473–1480. doi:10.1002/qj.631

Neff W, Helmig D, Grachev A, Davis D (2008) A study of boundary layer behavior associated with high NO concentrations at the South Pole using a minisodar, tethered balloon, and sonic anemometer. Atmos Environ 42(12):2762-2779

Nieuwstadt FTM (1984) The Turbulent Structure of the Stable, Nocturnal Boundary Layer. J Atmos Sci, 41, 2202–2216. doi:http://dx.doi.org/ 10.1175/1520-0469(1984)041<2202:TTSOTS> 2.0.CO;2

Obukhov AM (1949) Structure of the temperature field in a turbulent flow. Izv Acad Nauk SSSR Ser Geogr Geofiz 13:58-69

Petenko I, Mastrantonio G, Viola A, Argentini S, Pietroni I (2012) Wavy vertical motions in the ABL observed by sodar. Boundary-Layer Meteorol 143:125-141. doi:10.1007/s10546-011-9638-9

Petenko I, Pietroni I, Casasanta G, Argentini S, Viola A, Mastrantonio G (2013) Thermal turbulence in the very stable boundary layer: sodar observations at Dome C, Antarctica. Geophysical Research Abstracts, V.15, EGU2013-9442, EGU General Assembly, Austria, Vienna, April 2013

Petenko I, Argentini S, Pietroni I, Viola A, Mastrantonio G, Casasanta G, Aristidi E, Bouchez G, Agabi A, Bondoux E (2014) Observations of optically active turbulence in the planetary boundary layer by sodar at the Concordia astronomical observatory, Dome C, Antarctica. Astron Astrophys 568, A44: 1-10. doi:10.1051/0004-6361/201323299

Petenko I, Argentini S, Kallistratova M, Mastrantonio G, Viola A, Sozzi R, Casasanta G, Conidi A (2015) Spatio-temporal pattern of the surface-based turbulent layer during polar winter at Dome C, Antarctica as observed by sodar. 15th EMS Annual Meeting & 12th European Conference on Applications of Meteorology (ECAM), Sofia, 7-11 September 2015

Petenko I, Argentini S, Casasanta G, Kallistratova M, Viola A (2016) Wavelike structures observed in the turbulent layer during the morning development of convection at Dome C, Antarctica. Boundary-Layer Meteorol 161:289–307. doi:10.1007/s10546-016-0173-6

Pietroni I, Argentini S, Petenko I, Sozzi R (2012) Measurements and parametrizations of the atmospheric boundary-layer height at Dome C, Antarctica. Boundary-Layer Meteorol 143:189-206. doi:10.1007/s10546-011-9675-4

Pietroni I, Argentini S, Petenko I (2014) One year of surface-based temperature inversions at Dome C, Antarctica. Boundary-Layer Meteorol 150:131-151. doi:10.1007/s10546-013-9861-7

Salmond JA, McKendry IG (2005) A review of turbulence in the very stable boundary layer and its implications for air quality. Prog Phys Geogr 29:171–188

Schumann U, Gerz T (1995) Turbulent mixing in stably stratified shear flows. J Appl Meteorol 34:33–48

Seaman NL, Deng A, Stauffer DR (2002) Evaluation of a meteorological model for inter-regional transport. Final Report CRC Project No. A-28. Pennsylvania State University. http://www.crcao.com/reports/recentstudies00-02/A-28%20Final%20Report.PDF

Smedman A (1988) Observations of a multi-level turbulence structure in a very stable atmospheric boundary layer. Boundary-Layer Meteorol 44:231–253. doi:10.1007/BF00116064

Sorbjan Z (2006) Local structure of turbulence in stably stratified boundary layers. J Atmos Sci 63:1526-1537

Sorbjan Z (2010) Gradient-based scales and similarity laws in the stable boundary layer. Q J R Meteorol Soc 136(650A):1243–1254

Sorbjan Z, Grachev AA (2010) An evaluation of the flux–gradient relationship in the stable boundary layer. Boundary-Layer Meteorol 135(3):385–405

Sun J, Lenschow D, Burns S, Banta R, Newsom R, Coulter R, Frasier S, Ince T, Nappo C, Balsley BB, Jensen M, Mahrt L, Miller D, Skelly B (2004) Intermittent turbulence in stable boundary layers and the processes that generate it. Boundary-Layer Meteorol 110:255-279

Sun J, Mahrt L, Banta RM, Pichugina YL (2012) Turbulence regimes and turbulence intermittency in the stable boundary layer during CASES-99. J Atmos Sci 69:338-351. doi:http://dx.doi.org/10.1175/JAS-D-11-082.1

Sun J, et al. (2015) Review of wave-turbulence interactions in the stable atmospheric boundary layer. Rev Geophys 53:956–993. doi:10.1002/2015RG000487

Tatarskii VI (1971) The effects of the turbulent atmosphere on wave propagation. Israel Program for Scientific Translations, Jerusalem, 472 pp

Van Hooijdonk IGS, Donda J, Clercx H, Bosveld F, van de Wiel BJH (2015) Shear capacity as prognostic for nocturnal boundary-layer regimes. J Atmos Sci 72:1518–1532. doi:10.1175/JAS-D-14-0140.1

Van de Wiel BJH, Moene A, Hartogensis O, de Bruin HAR, Holtslag AAM (2002a). Intermittent turbulence in the stable boundary layer over land. Part I: A bulk model. J Atmos Sci 59:942-958

Van de Wiel BJH, Moene A, Ronda RI, de Bruin HAR, Holtslag AAM (2002b) Intermittent turbulence in the stable boundary layer over land. Part II: A system dynamics approach. J Atmos Sci 59:2567-2581

Van de Wiel BJH, Moene A, Hartogensis O, de Bruin HAR, Holtslag AAM (2003) Intermittent turbulence in the stable boundary layer over land. Part III: A classification for observations during CASES-99. J Atmos Sci 60:2509-2522

Van Ulden AP, Holtslag AAM (1985) Estimation of atmospheric boundary layer parameters for diffusion applications. J Climate Appl Meteorol 24:1196-1207. doi:10.1175/1520-0450(*1985*)024<1196:EOABLP>2.0.CO;2

Vignon E, van de Wiel BJH, van Hooijdonk IGS, Genthon C, van der Linden SJA, van Hooft JA, Baas P, Maurel W, Traullé O, Casasanta G (2017a) Stable boundary-layer regimes at Dome C, Antarctica: observation and analysis. Q J R Meteorol Soc 143(704):1241–1253, Part A. doi:10.1002/qj.2998

Vignon E, Genthon C, Barral H, Amory C, Picard G, Gall´ee H, Casasanta G, Argentini S (2017b) Momentum and heat flux parametrization at Dome C, Antarctica: A sensitivity study. Boundary-Layer Meteorol 162(2):341–367. doi: 10.1007/s10546-016-0192-3

Zilitinkevich SS, Elperin T, Kleeorin N, Rogachevskii I (2007) Energy- and flux-budget (EFB) turbulence closure model for stably stratified flows Part I: steady-state, homogeneous regimes. Boundary-Layer Meteorol 125(2):167–191

Yamada T (1976) On the similarity functions A, B and C of the planetary boundary layer. J Atmos Sci 33:781–793